Surface Emitting Semiconductor Laser

Thermal and Radiation Analysis

By

Xiaodong Wang

Submitted in Partial Fulfillment of the Requirements for the Degree of

Master of Science

(Electrical and Computer Engineering)

UNIVERSITY OF WISCONSIN – MADISON

SEP 2013

Surface Emitting Semiconductor Laser

Thermal and Radiation Analysis

By

Xiaodong Wang

Under the supervision of Professor Luke J. Mawst

At the University of Wisconsin – Madison

Approved by _____

Luke J. Mawst

Date _____

Abstract

This paper discusses the topic of semiconductor laser, focused on two types of surface emitting laser: Vertical Cavity Surface Emitting Laser and Quantum Cascade Laser. The author analyzes the temperature profile in VCSEL with current injection and index change induced by thermal expansion. This result is useful for thermal lensing effects. For the Quantum Cascade Laser, the author investigates Eigenfrequency solver by commercial software to calculate the radiation loss for different type of grating and explain the trend of radiation loss as grating depth increases. Different types of grating influences are conducted later. There are also some graphs about calibration and measurement for etching and deposition of device. These are important parameters for future device fabrication. At last, the author suggests some future work in design and device fabrication.

Acknowledgments

I would like to thank Professor Mawst for his guidance and encouragement throughout my graduate program. You have continued to motivate me through the hard times and helped me to achieve my goals.

I would also like to thank all of the members working in Prof. Mawst's research group for their support. I especially want to thank Jeremy Kirch, Colin Boyle, Toby Garrod, Chris Sigler, Chun-chieh Chang, Shuang Mao, Taewan Kim and Yinggang Huang for all of their help and advice during my time in Madison. I would like to appreciate those valuable suggestions from Professor Botez in Surface Emitting Quantum Cascade Laser design.

I highly appreciate some students and staff in University of Wisconsin-Madison who train me cleanroom facilities and help me set up experiments. I could not forget the help from Quinn Leonard, Hal Gilles, John Jacobs, Steven Ruder, Gareth Westler and Kamran Forghani. I would like to extend my thanks to Yunhan Chen in Stanford University for his contributions in VCSEL thermal diffusion modeling.

Finally, I would like to thank my family for their support and encouragement during this time. You have often believed in me more than I believed in myself, and I am truly grateful for everything you have done for me. I could not have done this without you.

Table of Contents

List of Figures

List of Tables

Nomenclature

Symbol	**Description**
VCSEL	Vertical Cavity Surface Emitting Laser
WPE	Wall Plug Efficiency
PPE	Power Plug Element
SEQCL	Surface Emitting Quantum Cascade Laser
DFB Laser	Distributed Feedback Laser
PBC	Periodic Boundary Conditions
PML	Perfect Matched Layer
ICP Etching	Inductively Coupled Plasma Etching
ECR Etching	Electron Cyclotron Resonance Etching
RIE	Reactive Ion Etching
PECVD	Plasma Enhanced Chemical Vapor Deposition
SEM	Scanning Electron Microscope
AFM	Atomic Force Microscope
GaAs	Gallium Arsenide
GaN	Gallium Nitride
InAlAs	Indium Aluminum Arsenide
InAs	Indium Arsenide
AlAs	Aluminum Arsenide
AlSb	Aluminum Antimony
AlAsSb	Aluminum Arsenide Antimony
InP	Indium Phosphide
AlGaAs	Aluminum Gallium Arsenide
InGaAs	Indium Gallium Arsenide
MOCVD	Metal Organic Chemical Vapor Deposition
MBE	Molecular Beam Epitaxy
LPE	Liquid Phase Epitaxy
PMMA	Polymethyl Methacrylate
ARROW	Antiresonant Reflecting Optical Waveguide
InGaP	Indium Gallium Phosphorus

Introduction

Overview

The semiconductor laser, in various forms, is the mostly widely used for all lasers. Every compact disc (CD) player contains one. Much of the world's long, and medium, distance communication takes place over optical fibers along which propagates the beams from semiconductor lasers. It is, by economic standards and degree of its application, the most important of all lasers. It distinguishes other kinds of lasers in small physical feature, low-power injection current, high fiber coupling efficiency and high speed modulation. There are great potentials in mass production and research benefits in studying semiconductor lasers.

Research Contributions

The major contribution of this research is to understand the physics behind surface emitting lasers. VCSEL temperature profile is conducted by commercial software COMSOL. Index change by thermal distribution is analysis for complete consideration of thermal lensing and free carrier diffusion. DFB SEQCL experiences different radiation loss due to design between grating depth and cladding layer thickness. Analysis about grating type influences on radiation loss is illustrated. Some cleanroom calibrations and measurements done for preparing future device fabrication is part of contributions in this paper.

Summary of Chapters

Chapter 1 consists of a summary of the state-of-the-art in semiconductor laser, mostly focused on surface emitting laser, VCSEL & QCL mechanisms. Some semiconductor physics background will be introduced here.

Chapter 2 describes thermal expansion, temperature profile inside 980 nm VCSEL device and brief analysis on influences in index change and free carrier absorption.

Chapter 3 presents simulation results for 4.6 microns SEQCL single-mode operation radiation loss, influences from grating depth, grating type and boundary conditions. This simulation is based on infinite element case by eigenfrequency solver.

Chapter 4 presents the experimental results of preparation for device fabrication. Dry etching, wet etching on InP sample for test and calibrations, metal deposition performances with related SEM images.

Chapter 5 contains a summary of research contributions and a discussion of future work in this area.

Chapter 1
Review of State-of-the-Art

1.1 Semiconductor Laser Introduction

The basic principle of laser operation is to take advantage of discrete quantum states of atomic systems. Argon ion laser and ruby laser are commonly used in life. Under the population inversion condition, stimulated emission from a higher quantum state to a lower quantum state is the origin of laser operation. In semiconductor laser, coherent emission originates by stimulated transition from a conduction band (higher energy) to a valence band (lower energy).

Semiconductor laser is first invented in 1961. The best-known application of diode laser is in optical communication systems. However, there are many other potential applications. In particular, semiconductor laser are being considered for high-speed optical recording, high-speed printing, single and multimode database distribution system and optical signal processing and data transmission, spectroscopy and some in medical applications. It distinguishes other types of laser in features as follow:

1.1.1 Small Feature Size

A small feature size (approximate 300um*50um*10um) makes semiconductor laser available to be incorporated into other devices or instrument. The world's smallest semiconductor laser is invented on a 5 nm thickness SiO_2 substrate with a 30 nm width of GaN/InGaN by researchers in University of Texas-Austin [1].

1.1.2 Low Injection Current

Low threshold and low injection current requirement (usually 15 mA at 2V is typical) makes semiconductor laser possible to drive it with conventional transistor circuitry.

1.1.3 High Efficiency

Semiconductor laser efficiency is defined as converting electric power to light. Actual operating efficiency exceeds 50%.

1.1.4 High Speed Modulation

The ability to modulate semiconductor laser output by direct modulation of the pumping current at rates exceeds 20GHz. This is of the major importance in high-data rate optical communication systems.

1.1.5 Integration for Mass Production

The possibility of integrating it monolithically with electric field effect transistors, microwave oscillators, bipolar transistors and optical components in semiconductors to form integrated optoelectronics circuits, lends itself a great potential to mass production.

1.1.6 Wide Range Wavelength

Semiconductor laser has the compatibility of its output beam dimensions with those of typical silica-based optical fibers and the possibility of tailoring its output wavelength to the low-loss (λ=1.55um), low dispersion (λ=1.31um) regions of such fibers. It is also available to tail its output wavelength to the blue spectral regime for display and the readout of high-density optical storage.

1.2 Device Physics and Classifications

1.2.1 Lasing Mechanisms

In semiconductor laser, lasing is made possible by the existence of a gain mechanism plus a resonant cavity under the condition of population inversion. In a conventional inter-band transition semiconductor laser, the gain mechanism is provided by light generation from the recombination of holes and electrons (Figure 1.2-1). The wavelength for output is determined by the bandgap of lasing materials. Holes coming from p side while electrons coming from n side, which are injected for recombination. Optical pumping and electric pumping are used to generate these carriers, for example, the forward-biasing p-n junction. In order to efficiently lasing light, active region of semiconductor laser, where the carrier recombination occurs, must be a direct bandgap material. Silicon cannot be used as active region material based on its indirect bandgap property while GaAs and InP are both suitable direct bandgap semiconductor materials. The surrounding carrier injection layers, so-called cladding layers, can be either direct or indirect bandgap materials.

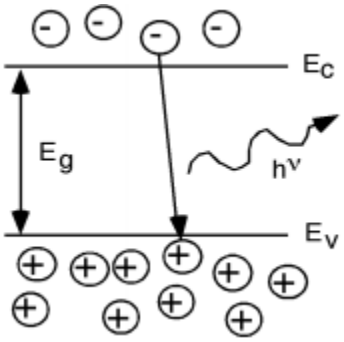

Figure 1.2-1 Schematic diagram of recombination of electrons and holes

Here we introduce this point of view from microscope side. We assume an optical beam at a frequency ω travels through the crystal. We use *a* representing an electronic state in the

conduction band and *b* representing an electronic state in the valence band. When separation of quasi-Fermi levels exceeds the transition energy, this incoming beam will induce downward $a \rightarrow b$ transitions for amplification as well as $b \rightarrow a$ for absorption. Net amplification of the beam results in the rate of $a \rightarrow b$ exceeds that of $b \rightarrow a$.

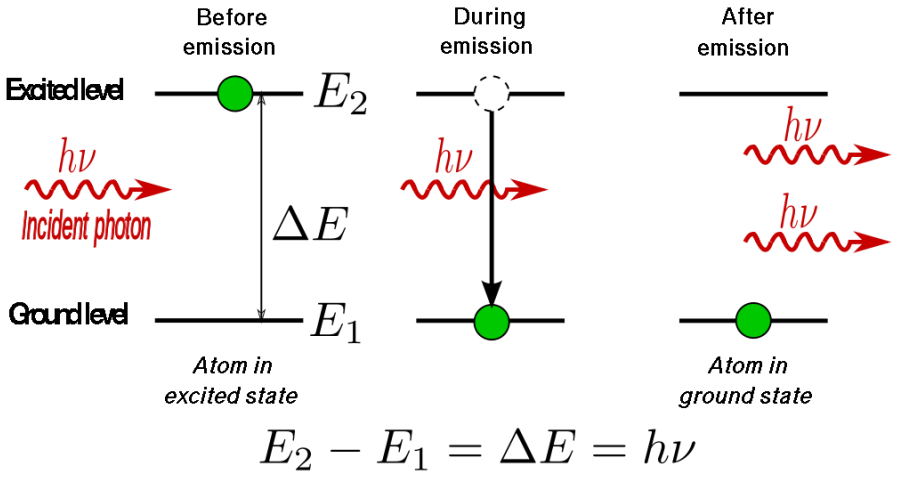

Figure 1.2-2 Schematic diagram of stimulated emission.

1.2.2 Material Growths and Fabrications

Three primary methods are used for growing semiconductor materials: liquid phase epitaxy (LPE), molecular beam epitaxy (MBE) and metal organic chemical vapor deposition (MOCVD), which the latter one is also called organic metal vapor phase deposition (OMVPE).

Most of the lasers fabricated in the earlier days of semiconductor lasers are done by LPE. It has been highly applied in mass production for commercial use; however, it is not suited for growing thin layer such as quantum wells lasers, because of lacking control and uniformity. MBE and MOCVD are better at this point.

In the simplest form, MBE is a form of vacuum deposition. Under the condition of proper temperature and ultrahigh vacuum environment, growth happens between thermal beams carrying atoms and substrates. Substrate is much cleaner in MBE than most of depositions or

growths only applied to single crystalline, with the whole process much controllable.

MOCVD is a chemical vapor deposition process. Gases flowing over the surface of a substrate form epitaxial layers. Most quantum well lasers are produced by MOCVD since it is a high throughput growth method suitable for production.

Double heterostructure (DH) laser can be fabricated by a variety of lattice-matched semiconductor alloys. The most two widely used combinations are GaAs/$Al_xGa_{1-x}As$ and InP/$In_xGa_{1-x}As_yP_{1-y}$. The former one holds the emitted wavelength from 0.78 um-0.87 um, while the latter one lasing wavelength is located in the range from 1.1 um-1.65 um.

Long wavelength semiconductor laser are of great interest in optical communication and molecular spectroscopy. Wavelength at near-IR is applied for optical storage applications. Some other materials are used for blue laser (short wavelength) for example, ZnSe-based laser emits 0.49 um at 77K. Similar to bipolar transistor or MOSFET device, semiconductor laser needs fabrication processing procedures in cleanroom. Basic steps include wafer processing, for example, photolithography, ion implantation, dry etching (mostly plasma etching), wet etching, deposition (Chemical/Physical vapor deposition), scribing, packaging. After devices are fabricated, we need test for its performance. During fabrication time, other techniques like scanning electron microscope, atomic force microscope, photoluminescence and electron-luminescence also needed for calibration, measurement and evaluation.

1.2.3 Quantum Well Lasers

Active Region in a DH laser is usually quite wide (>100 nm) that we do not need consider any quantum effects happening. In this case the conduction band and valence band is continuous. Density of states for energy E per unit volume per unit energy is:

$$D(E) = \sum_{t=l,h} \frac{m_r^i}{\pi^2 \hbar^3} \sqrt{2m_r^i (E - E_g)}, E > E_g \tag{1.2-1}$$

Where E_g is bandgap energy, $\hbar$ is plank constant divided by 2 π , *l* and *h* refers to light and heavy holes, m_r is effective mass of transition which is defined as:

$$\frac{1}{m_r} = \frac{1}{m_c} + \frac{1}{m_v} \tag{1.2-2}$$

Where m_c is conduction band mass and m_v is valence band mass.

If active region is very thin, then quantum effects would become important. When it becomes quite narrow, we name it quantum well structures (typically less than 20nm). In such a strucute, Schrödinger equation solutions show the formation of a discrete energy levels instead of continous energy bands of bulk materials. This quantization of energy levels will change the density of states into subbands of multiple quasi two-dimensional density of states. Another important function is Fermi occupation function, which describes the probability of carriers and their distribution in energy within the bands.

Some real physical limitations need to be considered in this decution. We often use Γ as optical confinement factor, M as matrix element for the transition between conduction band and valence band, N is carrier density of either electrons or holes. Γ is defined as the ratio of the light intensity of the lasing mode within the active region to the total intensity overall space, *g* is modal gain. Related formulas are listed as follow:

$$f_c(E_c, N) = \frac{1}{1 + \exp((E_g + E_c - F_c)/kT)} \tag{1.2-3}$$

$$f_v(E_v, N) = \frac{1}{1 + \exp(-(E_v - F_v)/kT)} \tag{1.2-4}$$

$$g(E,N)\alpha \frac{\Gamma D(E)|M|^2 (f_c(E,N)-f_v(E,N))}{E} \quad (1.2\text{-}5)$$

Threshold is another concept we need to introduce for discussion of device performance. The threshold current density (current divided by the length and width of the stripe) is a more meaningful measure of relative value of the lasing material gain than is current. It depends on material selection and laser geometry used (i.e. cavity length). Several factors are involved for current density calculation: reflectiveness of mirrors, absorption coefficient and transparency current density. Transparency current density is the value of current density when modal gain is zero. Compare only a single QW laser and DH laser, in most of cases QW laser has low current density, the end loss can be reduced by the use of high-reflectivity coating [2]. The combination of a single QW active region with a narrow stripe and high-reflectivity coating has allowed the realization of low threshold while high temperature operation. Another advantage of a QW structure is located in the lasing wavelength, which determined by bulk bandgap plus the first quantized energy levels. This can be changed by quantum well thickness. Strained QW structures give another degree of freedom for altering the energy bandgap and transition energy.

1.2.4 High Power Diode Lasers

In this section, we will introduce techniques for achievement of single mode operation high-power diode laser. Recently, quantum well lasers using the separate carrier optical confinement and ridge waveguide geometries have been used for producing power levels in excess of 700 mW operating in a single spatial mode. Such laser structures have properties of low threshold current density and low internal absorption losses, thus permitting higher-power operation.

To briefly introduce, we focus on several approaches for performing one of the most significant concerns: achieving high-power operation and high reliability of lateral lasing mode. Four approaches have been listed here: (1) increasing the lasing spot size, both perpendicular to and in the plane of the junction, and at the same time introducing a mechanism for discriminating against higher order modes; (2) eliminating or reducing the facet absorption by using nonabsorbing mirrors (NAM); (3) using laser arrays and unstable resonators to increase mode volume; (4) modifying facet reflectiveness by a combination of high-reflectivity and low-reflectivity dielectric coatings. Figure 1.2-2 is a plot for applications of different diode techniques with each output power versus cw current.

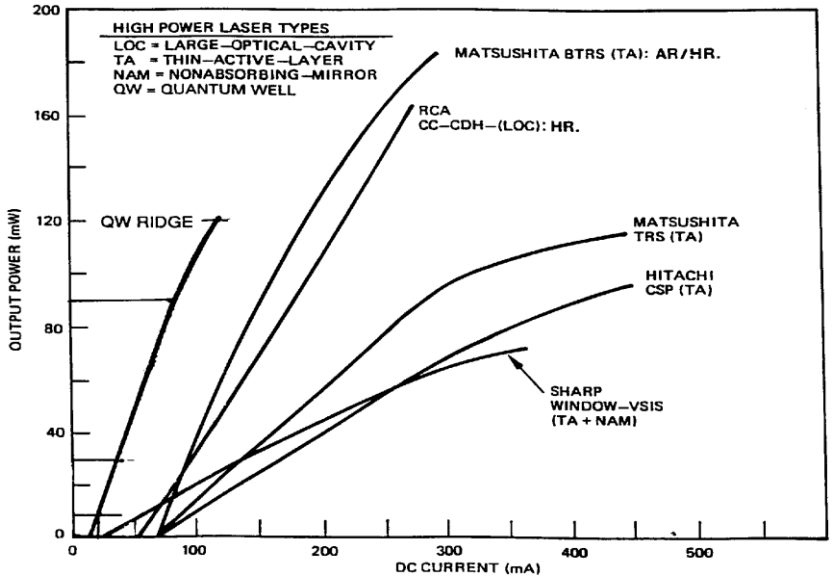

Figure 1.2-3 Plots illustrating output power versus cw current for high-power laser

Phase-locked array design is a practical method to overcome the problem that far-field pattern produced is not diffraction-limited and brightness reduced for wide emission aperture lasers. This is due to the happening of multimode generations and lateral-mode instabilities. Scifres and co-workers first reported on the phase-locked operation of a monolithic array

consisting of five closely coupled proton-bombarded lasers. Later, resonant phase-locking of leaky-mode elements is used for control mechanism of laser arrays. This technique has been widely used in recent modeling and fabrication [3].

Phase-locked array design is a most practical method to overcome the problem that far-field pattern produced is not diffraction-limited and brightness reduced. This is due to the happening of multimode generations and lateral-mode instabilities. Scifres and co-workers first reported on the phase-locked operation of a monolithic array consisting of five closely coupled proton-bombarded lasers. Later, resonant phase-locking of leaky-mode elements is used for control mechanism of laser arrays. This technique has been widely used in recent modeling and fabrication.

1.2.5 Surface Emitting Laser

Traditional laser, as stated in previous section, requires a pair of parallel facets for delineating the laser cavity. In this section, we describe the laser structures and fabrication techniques which allow light to emit perpendicularly to the junction plane, namely, surface-emitting lasers (SEL). There are three designs for surface-emitting lasers and arrays: (1) in-plane laser with 45 ° mirror; (2) vertical cavity laser; (3) in-plane laser with a distributed grating out-coupler.

Integrating with a 45 ° mirror requires a wafer processing of two 90 ° laser mirrors as well as a 45 ° mirror for deflecting the laser output from junction plane as shown in the figure. Dry etching techniques such as reactive ion etching (RIE), chemical assisted ion beam etching (CAIBE) and ion beam milling are usually used for fabrication. This approach takes use of well-

established layer structure growth. Laser performance relies on optical quality and reliability of the facet mirrors formed.

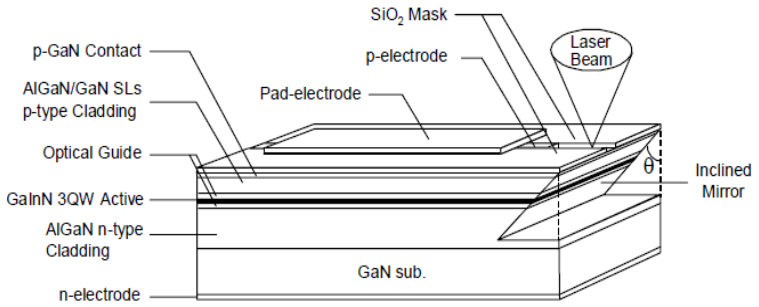

Figure 1.2-4 Schematic of integrating 45 °surface emitting laser. The guided light propagated reflects at the inclined mirror of the surface normal [4].

Distributed feedback (DFB) and distributed Bragg reflector (DBR) lasers are proposed and demonstrated in the early 1970s. First-order diffraction will be normal to grating surface compared with the second-order one. The critical issue involved in the fabrication is of the gratings with a period around 200 nm level. Another technique involved is direct electron-beam writing which is effective for design iterations. Development of DBRs with second-order gratings for surface-emitting lasers occurred rapidly with the U.S. Air Force pilot program [5]. Arrays of lasers with residual in-plane light injection across neighboring lasers for coherent operation.

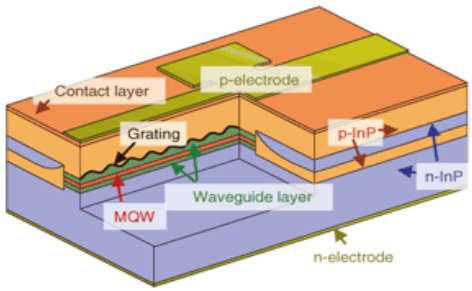

Figure 1.2-5 Schematic of InP based typical DFB laser

Vertical cavity laser reduces the cavity length down to 10 μm, which needs to have a pair of very high reflectively mirrors. Researchers in Tokyo Institute of Technology have used a thin metal-film and or a quarter-wavelength stack of dielectric layers of high- and low-index material. Larger than 99.9 percent reflectivity can be attained due to recent development of epitaxy growth conditions by either MBE or MOCVD. To maximize the modal gain, one can locate the standing wave field peak at the thin quantum well active region to form a resonant periodic gain structure. Section 1.3 will be focused on one specialized type-Vertical Cavity Surface Emitting Laser (VCSEL).

1.3 Vertical Cavity Surface Emitting Laser

As mentioned in last section, here is basic structure and material introductions of VCSELs. Chapter 2 will focus on VCSEL thermal analysis specified at relationship between injection current and temperature profile.

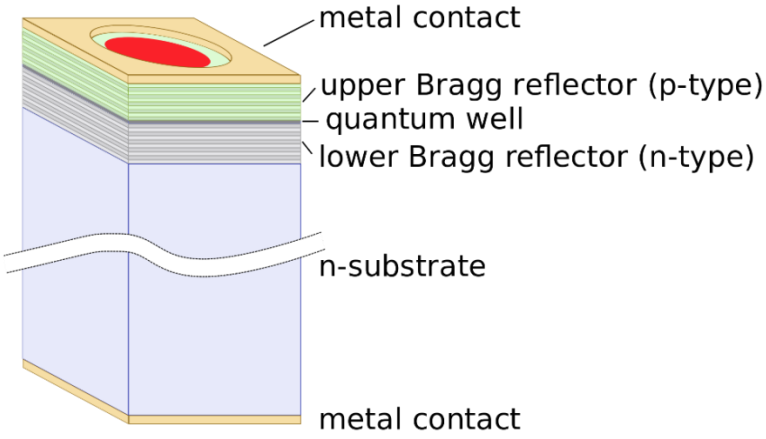

Figure 1.3-1 A simple diagram for VCSEL structure

1.3.1 Benefits from VCSELs

VCSEL belongs to Surface Emitting Laser (SEL), where laser diode with beam emission is perpendicular from the top surface, opposite to conventional edge-emitting semiconductor lasers which emit from surfaces formed by cleaving the individual chip out of a wafer. Several advantages about VCSELs are as follow: VCSELs can be tested at several stages throughout every process step to check for material quality and step correctness. However, in edge-emitting laser, testing can be only available until the end of production process. If it does not function properly, then production time and processing materials have been wasted. Additionally, tens of thousands of VCSELs can be processed simultaneously on the same wafer because they emit the beam perpendicular to the active region of the laser as opposed to a parallel edge emitter.

1.3.2 DBRs and Material Systems in VCSELs

In VCSEL structure, the most feature structure is DBRs parallel to wafer surface with an active region consisting several quantum wells for light generation. The planar DBRs are composed of layers with alternating high- and low-refractive indices. Each layer is within a thickness of quarter of the wavelength when the laser light in the material. Quarter-wave stacks reach the reflectiveness above 99%. This design is to balance the short axial length of the gain region. Upper and lower mirrors are doped as p-type and n-type semiconductor materials, forming a diode junction. Some even more complex structure has doped regions embedded between DBRs to make electrical contact arriving at active region, so that electric power loss decreased. Active region is pumped with a shorter wavelength, external light source. For emitting light between 650nm to 1300nm, DBRs are formed by GaAs/$Al_xGa_{1-x}As$ system. As the composition changes, lattice constant of material does not vary strongly but the refractive indices change a lot. Another problem is that, oxide comes along as aluminum increases, enabling a low threshold because oxide can be used to restrict the current. For longer wavelength above 1300nm, InP is fixed in active region. 1310nm VCSELs are desirable as the dispersion of silica-based optical fiber is minimal in this range.

1.4 Quantum Cascade Laser

Quantum Cascade Laser (QCL) is first demonstrated in 1994 by scientist Federico Capasso, Carlo Sirtori, Alfred Cho etc. at Bell Laboratories [6]. This laser is aimed at mid- to far- infrared portion of electromagnetic spectrum emission.

QCL is unique from other semiconductor laser where it is achieved through the use of intersubband transitions in a repeated stack of semiconductor multiple quantum well heterostructures, not as in inter-band devices which rely on the recombination of electron-hole pairs across the material band gap.

1.4.1 Intersubband versus Interband Transitions in QCLs

As mentioned before, conventional semiconductor lasers generate light by a single photon being emitted when a high energy electron in the conduction band recombines with a hole in the valence band. The energy of the photon and hence the emission wavelength of laser diode is determined by the gap between conduction band and valence band (bandgap) of the material.

QCL however, does not rely on this mechanism to achieve light generation. Instead it comprises a periodic series of thin layers with varying material composition to form a superlattice which introduces a varying potential across the length of device. Actually it is a one-dimensional quantum well confinement and leads to splitting of bands into several electronic subbands. The key point in design is the thickness of layers, not only the material. By tuning the thickness from design, it is possible to tune the emission wavelength of QCL over a wide range in the same material system. What is more unique is that, once electrons undergo the intersubband transition and emit a photon in one period of superlattice, they can move to next

period of superlattice and continue useful for another photo generation or even more. This process of multiple travelling through QCL structure gives rise to the name “cascade” and makes efficiency larger for high-power output.

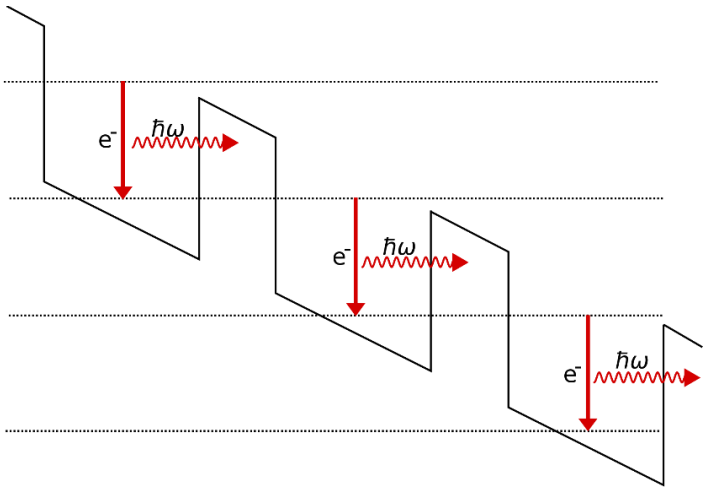

Figure 1.4-1 Electrons undergo intersubband transitions and photons emitted and then electrons tunnel to next period of structure and repeat the same process

1.4.2 Material Systems in QCLs

Similar to VCSELs, different materials systems will provide different emitting wavelengths. The first demonstrated QCL system is fabricated on an InP substrate with an InGaAs/InAlAs system. Devices made then showed a mid-IR spectral range with high-power above room-temperature, continuous wave emission. Short wavelength around 3μm for QCL device is fabricated with very deep quantum wells at 1.6eV deep for InGaAs/AlAsSb system. Aimed at 2.5 μm by InAs/AlSb system at 2.1eV deep QCL devices have also been observed. Recent research interests have been focused on terahertz region of spectrum. GaAs/AlGaAs based QCLs demonstrated by Sirtori proved that a varying quantum well depth depending on fraction of aluminum fraction is successful in THz region.

1.5 Conclusion

Most of this chapter focuses on background introduction of semiconductor laser, such as history, application, development and category. We introduce some basic processing steps used in semiconductor laser fabrication and material growth, physics behind them. Concepts such as quantum well laser, high-power diode laser and vertical emitting laser are stated in this chapter. Then we move on two specified types where research is developed: VCSEL and SEQCL. In the next chapter we will discuss the thermal simulation study of VCSELs.

Chapter 2
VCSEL Thermal Analysis

This chapter talks about Vertical Cavity Surface Emitting Laser two-dimensional and three-dimensional thermal modeling and related analysis about refractive index change with free carrier absorption phenomena. Most of contents will be focused on modeling by COMSOL Multiphysics, especially by means of mesh and sweeping to deal with high memory requirement.

2.1 Motivation of VCSEL Thermal Analysis

The thermal modeling work for VCSEL is an additional work for above threshold VCSEL research done through the collaboration between Troitsk Institute for Innovation and Fusion Research and University of Wisconsin-Madison. The work for calculating output power by changing number of DBR pairs and drive current is published on IEEE journal of selected topics in quantum electronics [7]. This simulated steady state temperature distribution within the device can be used to estimate a thermal lens, which will in turn impact the modal characteristics of the VCSEL array. In future studies, the thermal lens can be incorporated into the above threshold simulation model which is described in [7].

2.1.1 ARROW Structure

Antiresonant reflecting optical waveguide (ARROW) terminations are employed to reduce edge radiation losses of single antiguides, or of three-element antiguide arrays [8]. Effective index theory is applied here as a schematic diagram of arrangement. The ARROW terminations consist of high-index and low-index regions which have widths corresponding to an

odd-integer number of quarter-waves of the lateral leaky-wave radiation. The anti-resonant condition resonant will result in minimum radiation loss. To ensure that, arrays employing ARROW terminations must rely on suppressed modal gain and higher loss of non-resonant modes [9]. Non-uniformity of the refractive index was shown to strongly diminish the discrimination of unwanted modes at the index difference of about 0.002-0.004. What should be taken care of is that as the number of array elements increases, the tolerance to achieving resonance becomes tighter, making it more difficult to fabricate.

2.1.2 Thermal Effects

Current-induced self-heating of VCSELs has been identified as a major factor limiting their static and dynamic performance. Self-heating manifests itself as the premature saturation of the output power with increasing bias current, under cw operation. Subsequent saturation of the photon density in the active region limits VCSEL's modulation speed. The phenomena responsible for self-heating have received a great deal of attention, both experimentally and theoretically. Experimental studies on improving the thermal-limited dynamic performance have focused on reducing resistance, internal optical absorption and thermal impedance. Theoretical modeling of self-heating effects is a complex problem and involves taking into account various optical, electrical and thermal interactions for the specific VCSEL design under consideration [10].

Clearly, in order to effectively design optoelectronic applications incorporating VCSEL's, appropriate models are required which account for thermal effects, in particular the temperature-dependent threshold current and out-put power rollover identified above. The majority of such models to date have been largely numerical in nature, making use of detailed multidimensional

analysis for the description of VCSEL thermal behavior. For example, Nakwaski and Osinki have developed extensive two-dimensional models of thermal heating, while other researchers have incorporated finite element analysis of thermal effects into their comprehensive VCSEL simulations. Their models are both accurate and computationally intensive. This feature makes them unattractive for the computer-aided design of optoelectronic systems, which are typically composed of many photonic and electronic components.

2.2 Two Dimensional Layout of Thermal Model

Before moving to more complex three dimensional model of temperature model of VCSEL, we first make a simple two dimensional model as an introduction part. Comsol Multiphysics is a popular commercial software based on finite element analysis. It packages analysis, solver for various physics and engineering applications. The mathematical basis of Comsol Multiphysics is by solving coupled series of partial differential equations (PDEs). RF module and heat transfer module are mostly used in this research. For this chapter, heat transfer module will be applied as major modeling tool for temperature analysis.

It has been briefly introduced about VCSEL structure. DBRs play an important role of increasing reflection between quantum well layers. This requirement is due to limited length of active region. The VCSEL modelled in this chapter is based on three layers of GaAs/InGaAs quantum wells. Below and above quantum wells are confinement layers made of AlGaAs. Optical confinement layers on either side of active region layer confine the light emitted by the laser to the active region. Between the bottom confinement region and substrate is 32 pairs of n-DBR, while between the top confinement region and gold/air interface is 18.5 pairs of p-DBR.

This structure is optimized for best output light. The DBRs which act as mirrors are doped as p-type and n-type materials, forming a diode function. In some more complex structures, the p-type and n-type regions may be embedded between the mirrors, requiring a more complex semiconductor process to make electrical contact to the active region, but eliminating the electrical power loss in the DBR region.

DBRs are composed of GaAs/AlAs combinations. Each pair is a sum of quarter-wave length both GaAs and AlAs, defined by designed wavelength and refractive index. Above the laser device, there are two kinds of area, element region and interelement region. Two differences exist between them, element region top area is air while interelement is gold. Gold is used to absorb most of light within interelement region. At interelement region between the confinement layer and p-DBR there exist a layer of compensation layer, composed of very thin InGaP and GaAs. Compensation layer is also called spacer layer, each part has a 12nm thickness. The role of spacer layer is to create the differences between effective refractive index $\Delta n \sim 0.025$. This is the key point of antiguided VCSEL design. In antiguided VCSEL design, low index region has high optical gain. Previous simulations have shown that photonic lattice effect contributes to the low fundamental mode loss while higher order of leaky modes exhibit significantly higher loss.

2.2.1 VCSEL Structure Construction

To better illustrate the structure, three dimensional diagram for overall view of VCSEL has been added here with cross-section view of two dimensional diagram for element and interelement view.

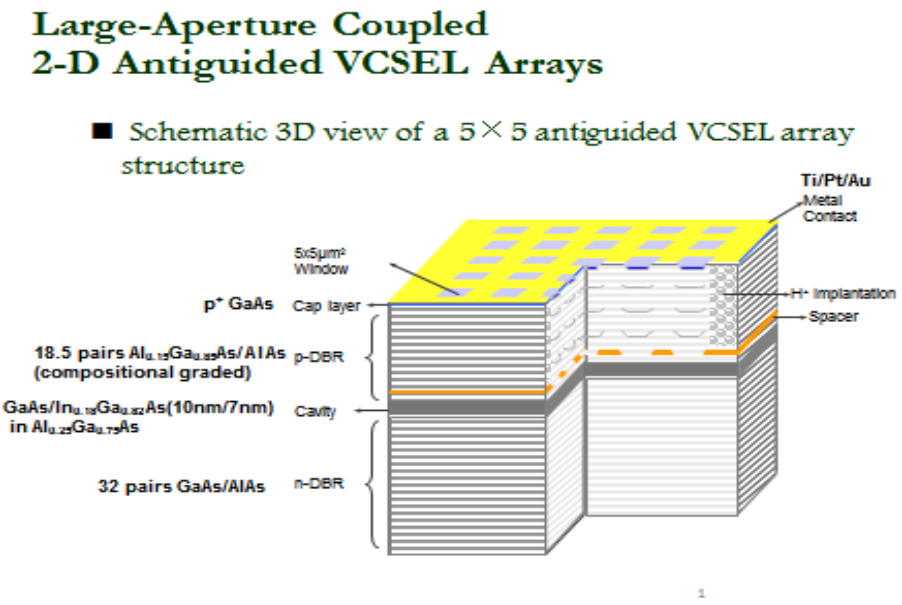

Figure 2.2-1 3D diagram for VCSEL overview structure

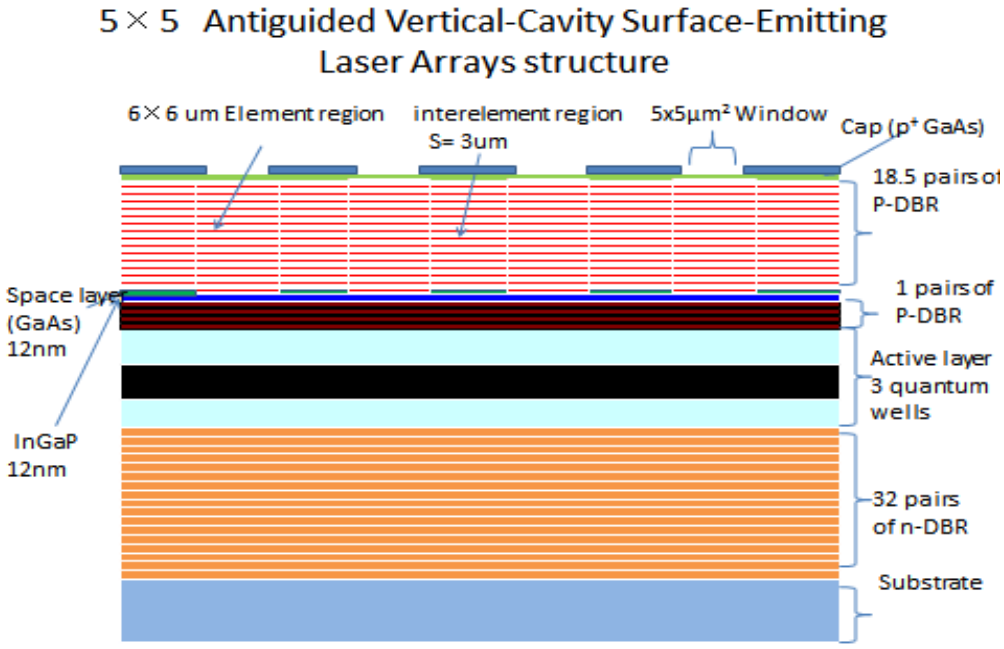

Figure 2.2-2 2D diagram VCSEL overview structure

Three parameters involved are for thermal study, such as thermal conductivity, density and heat capacity and constant pressure. As to constructing the model, refractive index of materials and thickness are necessary. Here is the table for listing all values.

Table 2.2-1: Parameters for VCSEL Thermal Model Construction

Material	Thermal conductivity (J/kg*K)	Density (kg/m^3)	Heat capacity at constant pressure (W/m*K)
GaAs	55	5320	330
AlAs	91	3760	450
AlGaAs	17.5	4930	360
InGaAs	6.756756	5376.6	260
InGaP	5.1282	4475	370
Au	301	19320	128
Air	0.0257	1.205	1005

Active region in this VCSEL structure is a three-layer quantum well InGaAs sandwiched between GaAs. Thickness of InGaAs is 7nm and 10nm for GaAs. Element width is 5μm and interelement is 3μm, which are based on design in previous above threshold reflecting boundary analysis.

Table 2.2-2 Dimensional Structures in VCSEL

Element Width (μm)	5	Interelement Width (μm)	3
GaAs Quantum Well Width (nm)	10	InGaAs Quantum Well Width (nm)	7
GaAs DBR thickness (nm)	69.6	AlAs DBR thickness (nm)	83.05
InGaP Space Layer (nm)	12	GaAs Space Layer (nm)	12

2.2.2 Heat Transfer Setting and Temperature Distributions

After constructing majority part of the structure, it is necessary to consider boundary condition in whole picture. Usually in the device there is a bulk substrate of which the edge has the same temperature as air. It is assumed that VCSEL is working under room temperature, so boundary of device is set to be around 293K, namely 20℃. The governing equation for thermal diffusion is:

$$\rho C_p u \bullet \Delta T = \nabla \bullet (k \nabla T) + Q \qquad (2.2\text{-}1)$$

Corresponding variables such as k is thermal conductivity, ρ is density and C_p is heat capacity at constant pressure. Q is defined as heat source which needs to be input. The definition of Q a formula involved wall plug efficiency (WPE), power per element (PPE), interelement width (iew), element width (ew), quantum well depth (h_well). The formula is as follow:

$$Q = \frac{PPE * 5 * (1 - WPE)}{(h\_well) * (iew + ew)}. \tag{2.2-2}$$

After modeling, results about temperature distribution has been attached here. It is obvious to see that highest temperature located at active region where it is heat source. To better compare the differences between quantum well and top p-DBR region, it is necessary to make a one-dimensional line scan through horizontal axis.

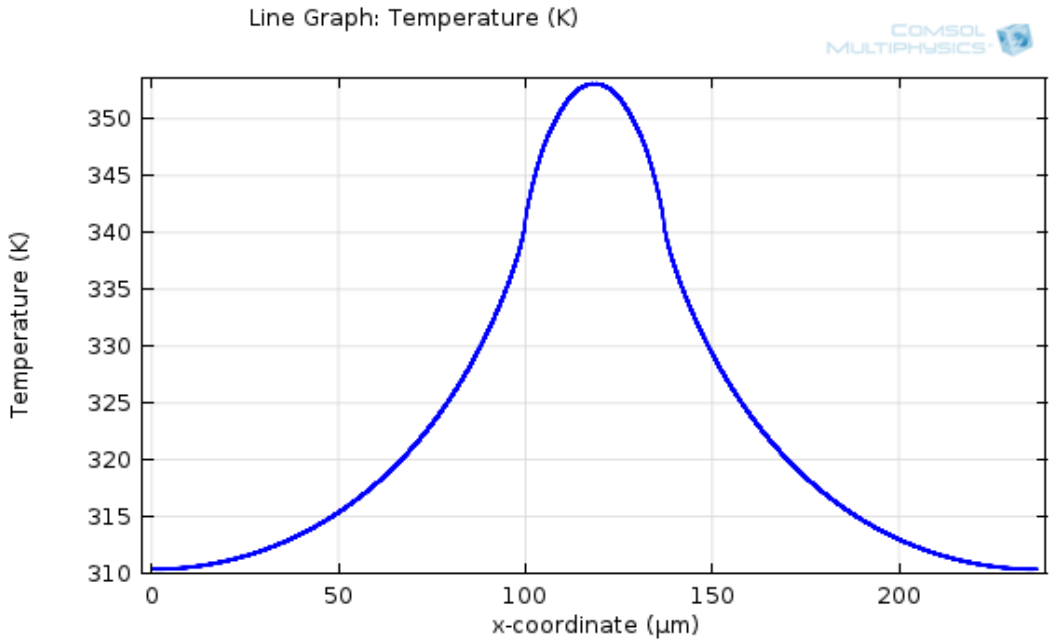

Figure 2.2-3 1D line scan of Active Region

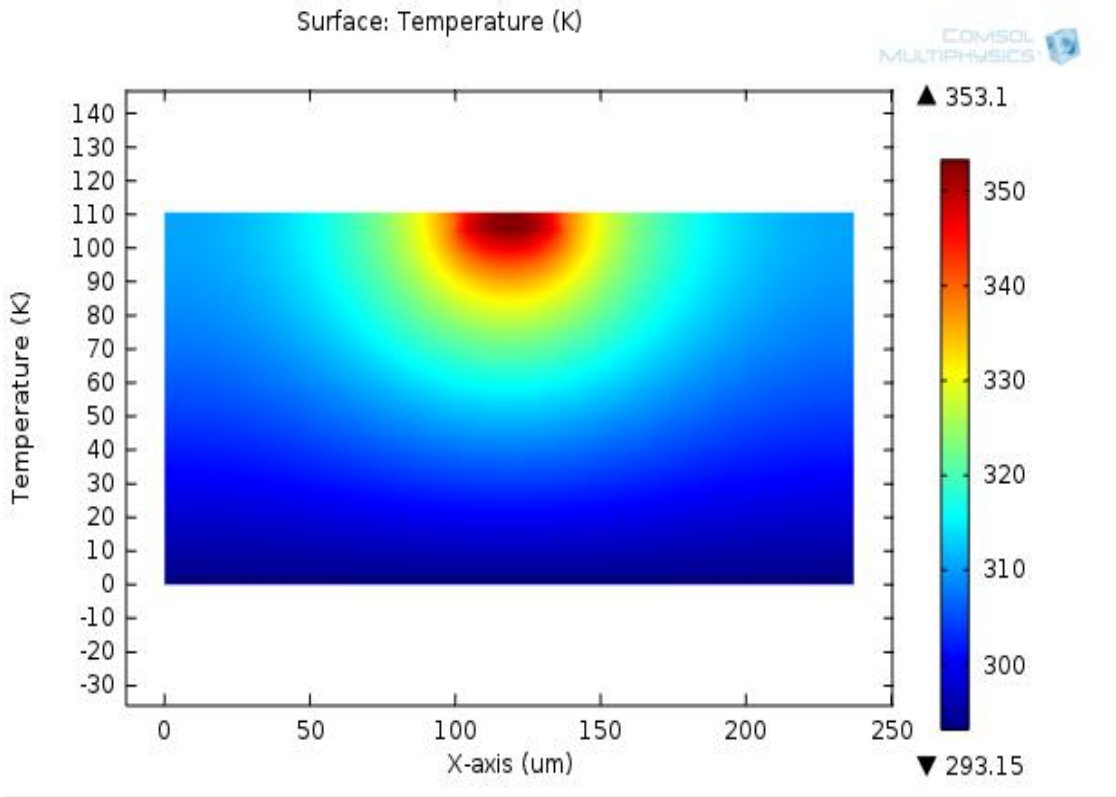

Figure 2.2-4 2D Surface temperature Profile of VCSEL

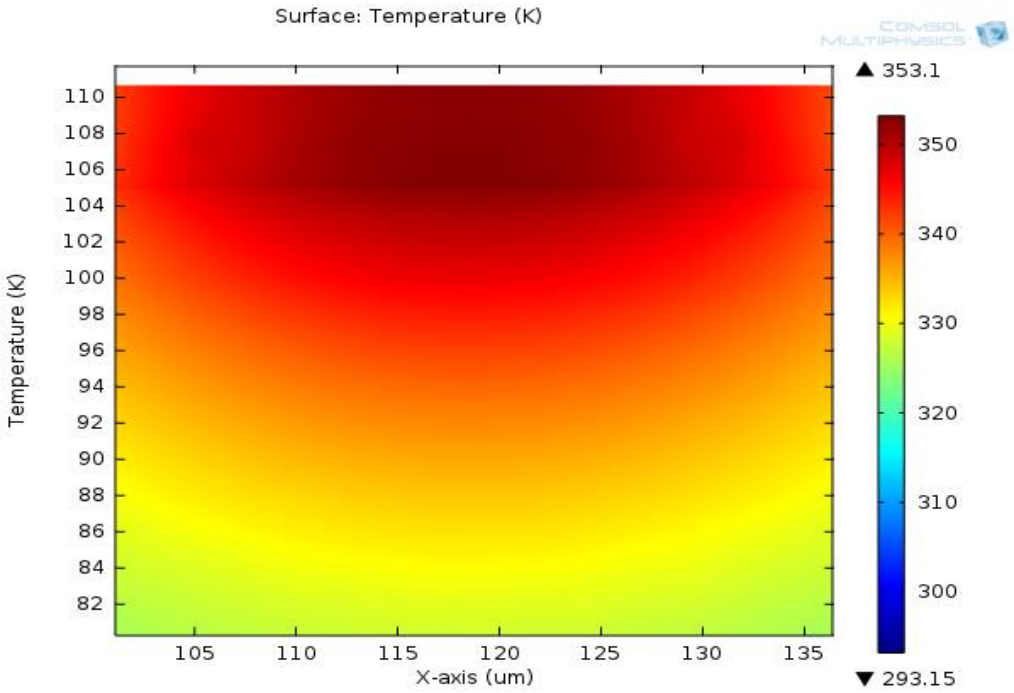

Figure 2.2-5 Detailed Part of Continuous Heat Source within Active region

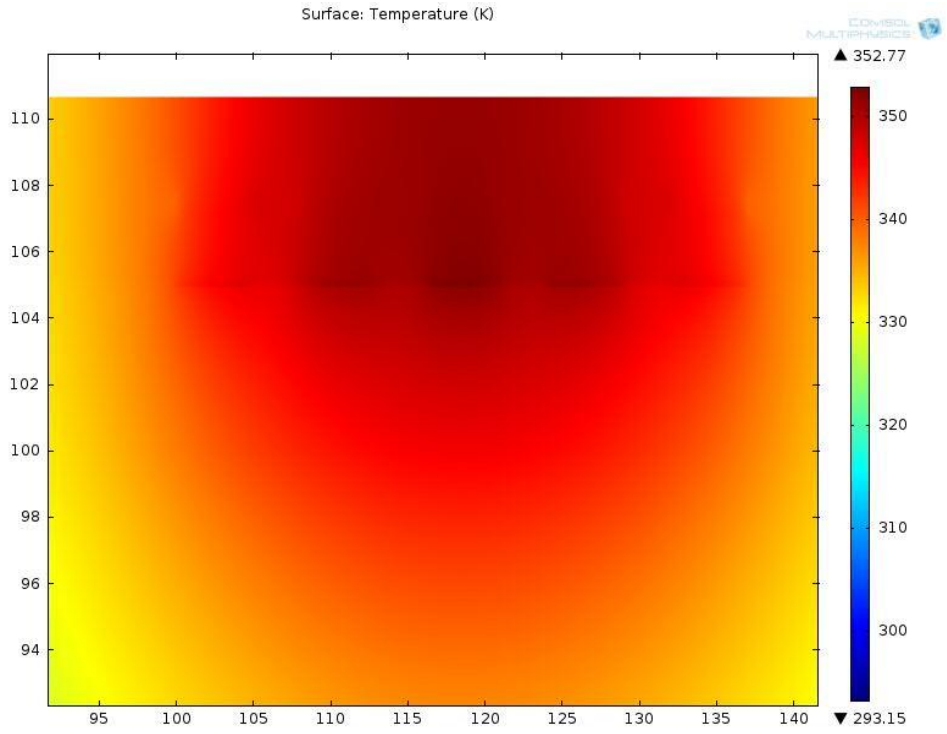

Figure 2.2-6 Detailed Part of Separate Heat Source within Active region

There are two kinds of heat source, one is continuous and the other is separate. Continuous heat source is buried within both elements and interelements, which is more close to reality, since current generally spreads into the interelement regions and contributes as a heat source. Because current could be injected into the device to element region, so between elements, there are not as much heat as that in active region, so based on that, real temperature inside device should be between continuous and separate heat source.

Considering the results from both kinds of heat source, it is easy to see that they both achieve at a temperature around 353K. As initial temperature is set at around 293K (room temperature), it will reach the conclusion that roughly 60K more compared with hottest part of device with boundary or heat sink. This will induce a thermal lensing effect which changes output light profile possibly. Differences between two kinds of heat source here is not much.

2.3 Three Dimensional Layout of Thermal Model

Last section we are describing the 2D model for VCSEL temperature profile construction. Here we move on to three dimensional model and some tricky points in model construction will be issued here for RAM save and fast processing.

Comsol Multiphysics is based on finite element analysis, which uses variation methods to minimize an error function and produce a stable state [11]. This method encompasses all the methods for connecting many sample element equations over small subdomains, to approximate a more complex equation over a larger region. Mesh in finite element analysis is defined as splitting of domains into smaller subdomains. The governing equations of a physics are then discretized and solved inside each of these subdomains. The way how to ensure the proper continuity of solution across the common interfaces between two subdomains, so that the approximate solutions inside various proportions can be put together to give a complete picture of fluid flow in the entire domain should be taken good care of. With proper setting, it would give a simple and memory saving of running a complex structure.

It would be very hard to evaluate the memory requirement for running such structure because inside this model, some part (active region) is within nanometer dimension. This requires the system meshing at minimum size and will cost a lot of memory usage. Then by the help from Comsol technical support, working planes and sweep meshing are introduced so that it is achievable to conduct three-dimensional model VCSEL thermal diffusion model running on server. The server used in this simulation has a 32GB RAM with Windows XP system. Before optimization, it will take more than 128GB estimated from Comsol software about memory

interface while after optimization, it only takes less than 10GB to run. Here several detailed pictures about working plane method and meshing is listed.

Compared with traditional method of constructing blocks, only one block is constructed here. Each layer is separated by different working plane. Parameters defined by different materials is contained within the information of each plane. For meshing, general meshing method is by creating tiny small triangular bodies. However, super high RAM requirement here does not allow this available. So it is done as creating triangular shape on one interface and then swept through the whole region. Because the model is constructed under one whole block, so there is no problem happening from boundary between different geometry. One thing needs to be taken care of is where the interface between interelement region and element region. Because they share a common boundary at *x-y* plane, sweeping needs to be done separately there. Construction of whole structure takes time but a good experience to under the mechanism to run Comsol.

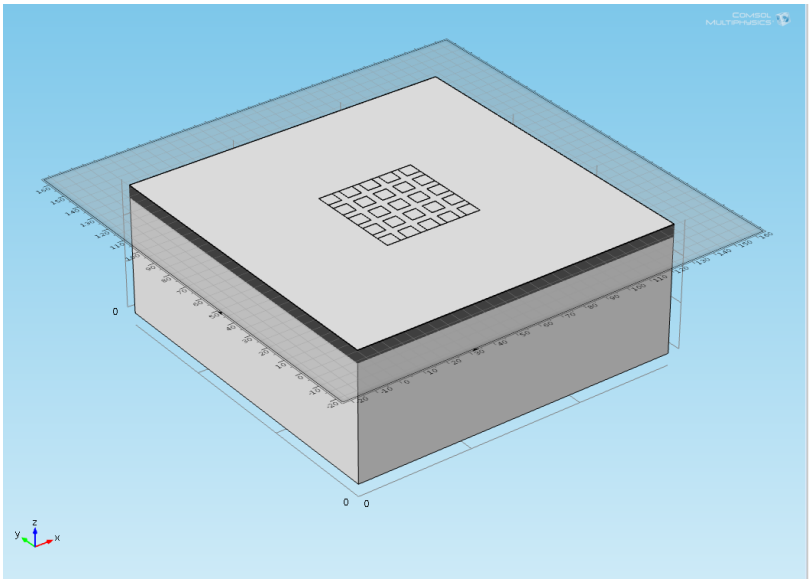

Figure 2.3-1 Overall Structure of Three-dimensional VCSEL Structure

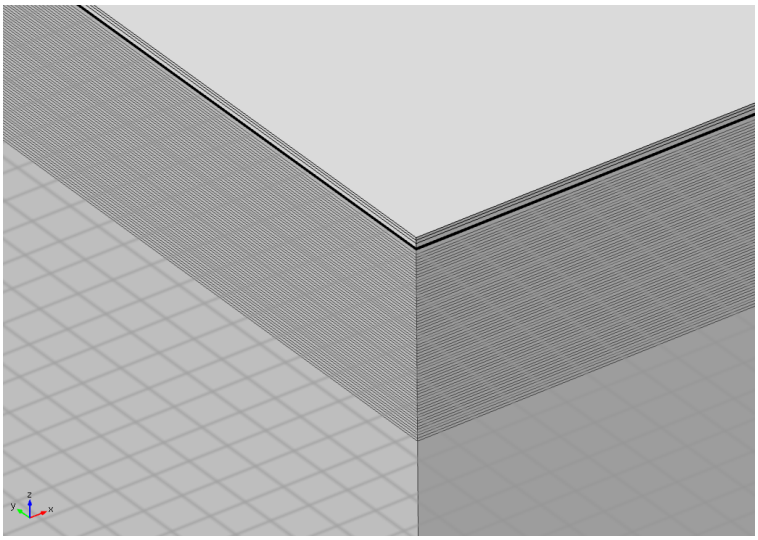

Figure 2.3-2 Detailed Structure of Three-dimensional VCSEL Structure (different working planes)

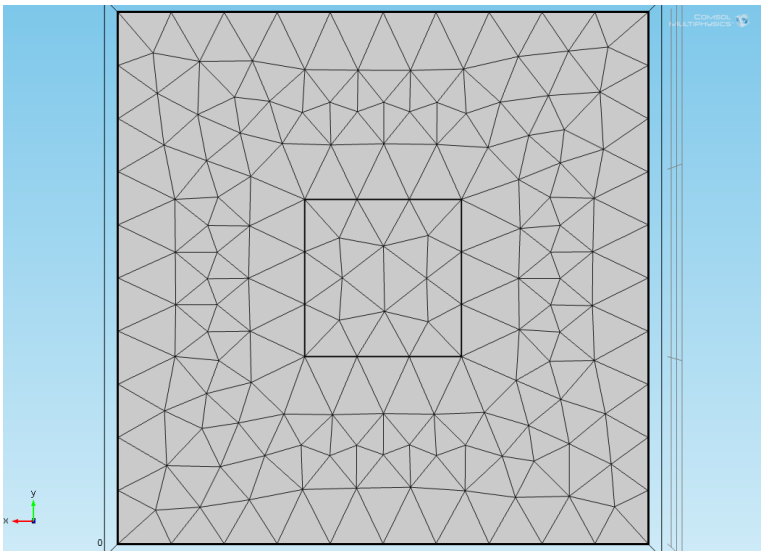

Figure 2.3-3 Bottom Meshing as Sweeping Source

After model is constructed, next step is to investigate the temperature profile within device. We set three different PPE as 0.005, 0.01 and 0.015. For simplicity, it is only necessary to see the differences on one PPE. At this time, two heat source are also set as uniform and separate heat source. We put the three-dimensional temperature with PPE=0.01 for both heat source types.

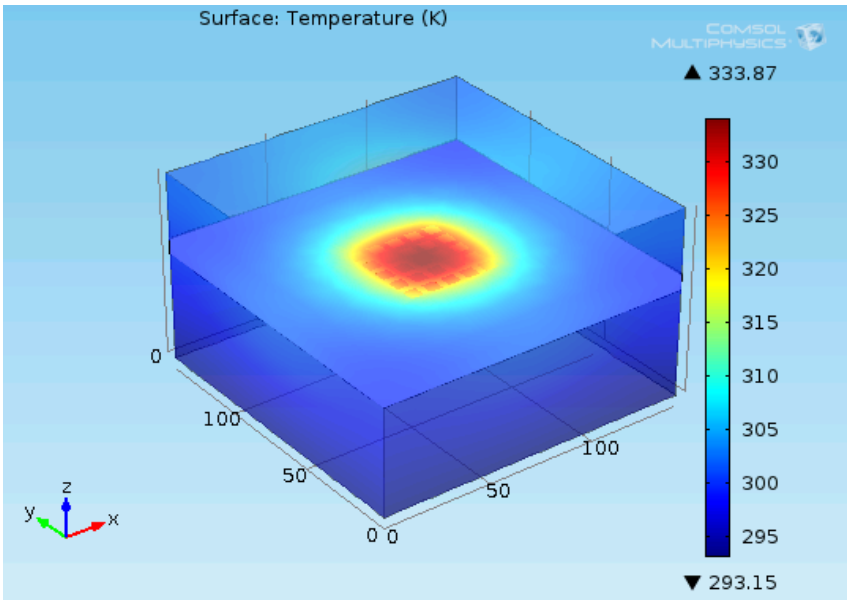

Figure 2.3-4 3D Surface temperature Profile of VCSEL (Separate Heat Source)

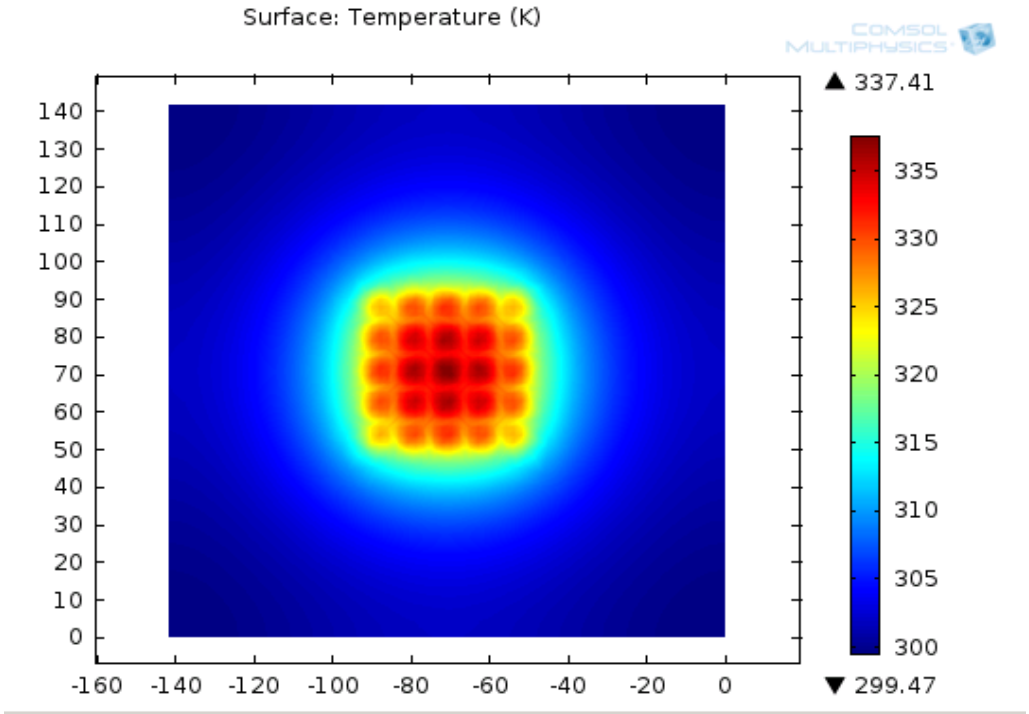

Figure 2.3-5 2D Surface temperature Profile of VCSEL through Active Region (Separate Heat Source)

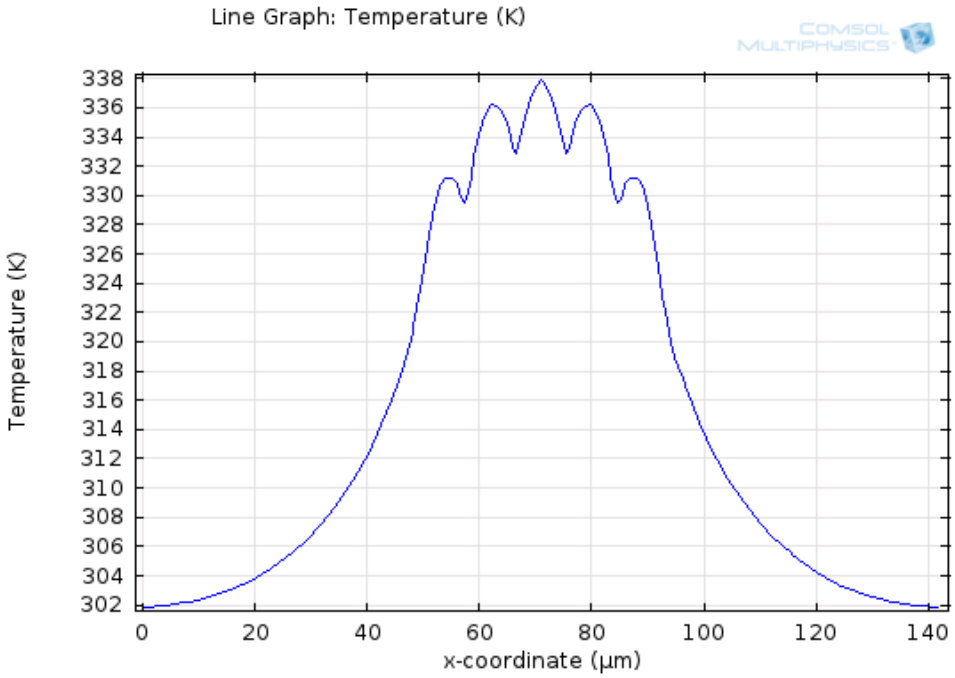

Figure 2.3-6 1D Surface temperature Profile of VCSEL through Active Region (Separate Heat Source)

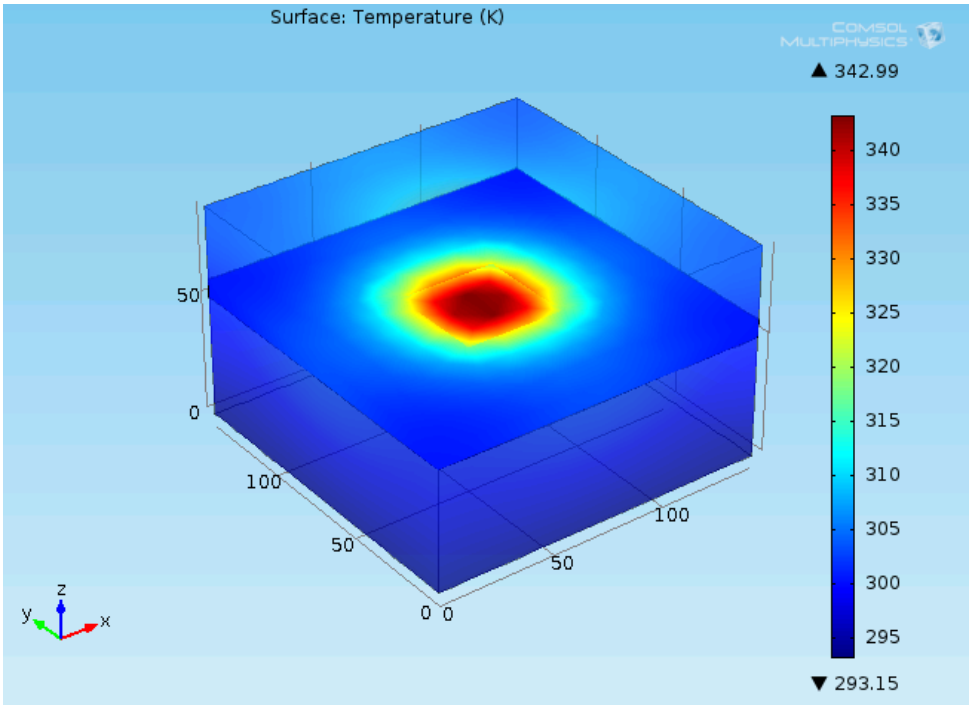

Figure 2.3-7 3D Surface temperature Profile of VCSEL (Uniform Heat Source)

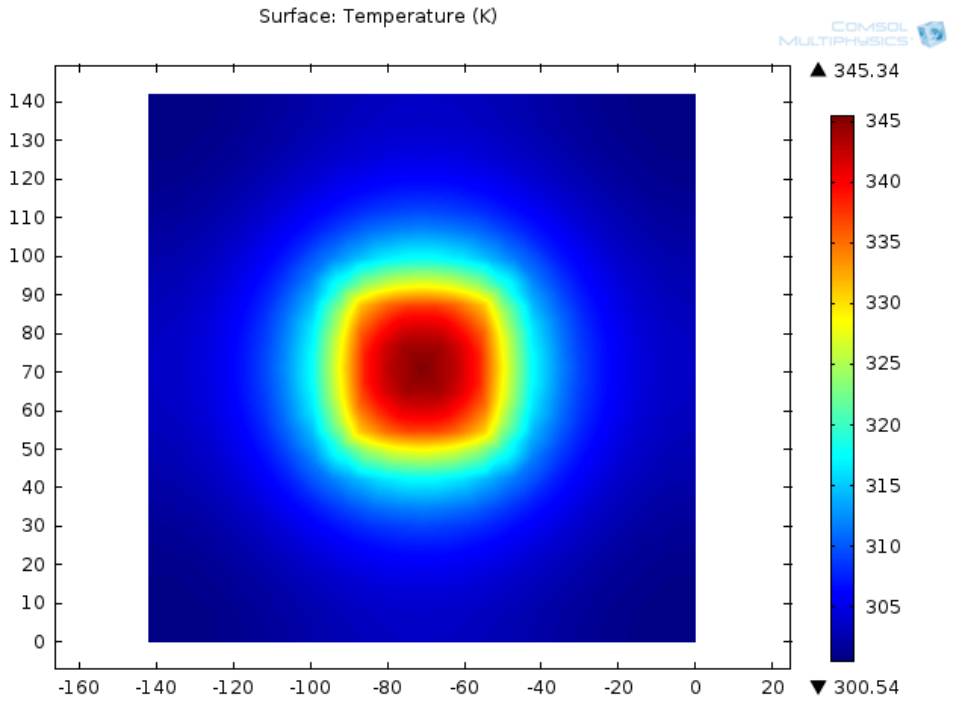

Figure 2.3-8 2D Surface temperature Profile of VCSEL through Active Region (Uniform Heat Source)

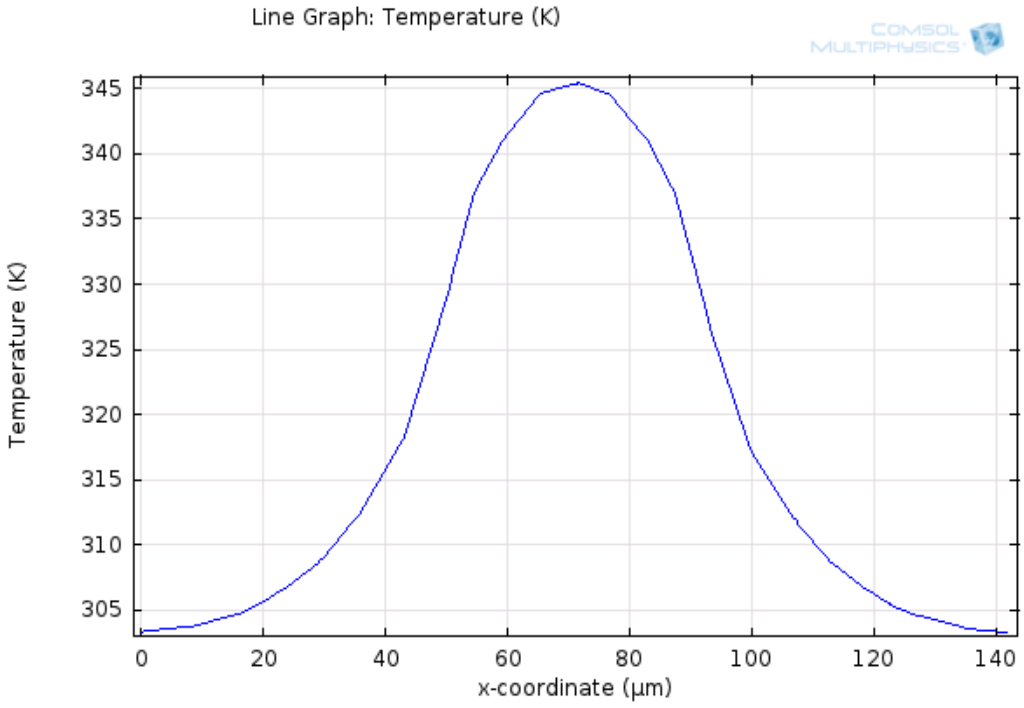

Figure 2.3-9 1D Surface temperature Profile of VCSEL through Active Region (Uniform Heat Source)

It is easy to see that both thermal model achieves a close temperature at around 342K. As we know, the real situation should be between both conditions, so it would be reasonable to predict that real temperature would be around 343K to 345K. The separate heat source one-dimensional plot shows a multi-local maximum points which matches the heat profile while uniform heat source shows a similar Gaussian profile.

2.4 Thermal Lensing Effects

To design a high performance VCSEL, the main issue is the tradeoff between low threshold and high quantum well efficiency. Low threshold primarily implies the high mirror reflectivity, fewer quantum wells and smaller device area. Assuming the ideal situation in which the LI curve is linear above threshold, the current required to achieve a given input power is simply related to both threshold and quantum efficiency.

Thermal lensing is induced by temperature gradients. In high-power lasers, the heating of the gain medium often causes a significant thermal lens through the following mechanism: (1) the gain medium is hotter on the beam axis, compared with the outer regions, typically causing some transverse gradient of the refractive index (thermal optics effect, quantified with the coefficient (dn/dt); (2) further index changes can be caused by thermally induced mechanical stress; (3) mechanical stress also lead to bulging of the end faces of the gain medium, so that these also cause lensing. This effect can be important for short laser crystals.

An in-depth analysis of thermal lensing requires advanced methods as finite element analysis (FEA) for the calculation of the temperature and stress fields in the laser. It is often advantages to use the more pragmatic approach of working with estimates based on various simplifying assumptions, which greatly reduce the effort required and still offer useful guidance

for experiments. The dependence of the power of the thermal lensing on the beam area can be different for other laser geometries. An at least partially longitudinal heat flow and this a reduction in thermal lensing may also be achieved with a transparent hear spreader. Thermal lensing can also be significant outside a laser resonator when a laser beam with high average power is sent through a transparent optical device such as a lens, a beam splitter or a protection window. As a result, the position of a focus behind such an element may depend on the optical power level. This can happen in high power laser cutting heads.

2.5 Conclusion

This chapter provides a detailed overview of thermal modeling for VCSEL. The breakthrough inside this chapter is to the use of thin-layer diffusion technique for super thin layer meshing in COMSOL Multiphysics. Under help from technical support, it is a great opportunity to learn how to deal with different type of geometry based on server configurations. Extremely thin layer is common in VCSEL device, even though this modeling is for thermal diffusion goal, this method would be great helpful to extend to RF module for electromagnetic wave analysis.

From the work done here, it would be promising to see the effects from thermal lensing and free carrier absorption by temperature profile. Also, the model constructed here can be applied to RF module for a complete set of research basis. As both module share a same geometry, it is possible to achieve multi-physics combination analysis for a specified device structure.

Chapter 3
Surface Emitting Quantum Cascade Laser

This chapter focuses on surface emitting quantum cascade laser modeling by Comsol Multiphysics and MATLAB.

3.1 Introduction of Surface Emitting QCL

It is briefly introduced about the working principle of QCL and DFB laser in Chapter 1. Surface emitting QCL is based on a second order grating of a DFB laser. During the last decade, significant improvements make QCLs interesting for many applications [12]. An important step for the use of these devices was the achievement of single mode emission. This is first demonstrated by processing DFB lasers an employing first-order grating, where a grating imposed on a top of the laser selects a single longitudinal mode within the gain spectrum of the device [13]. Within recent years, tunable single mode emission has been also achieved by grating-coupled external cavity QCLs [14].

QCLs are based on intersubband transitions, selection rules for transitions in quantum wells allow gain only for TM polarizations. Therefore conventional VCSEL design is not suitable for QCLs, so another approach must be taken. One successful method is to use two-dimensional photonic crystals. A DFB design where the feedback is given through a second-order Bragg grating etches into the surface of the larger ridge [15]. Such SE-QCLs have been realized in both InGaAs/InAlAs/InP and GaAs/AlGaAs system. Appropriate etching depths, a low loss top cladding and metallization of the grating peaks only, lead to high power surface emission for devices operating in the near-IR spectral region.

3.2 Theory and Modeling Set-up

3.2.1 Modeling Set-up and Parameters

In this chapter, an investigation of waveguide structure, grating height and shapes as well as far-field plot is carried out for a 4.6 μm surface emitting second-order DFB QCL structure.

It is a key issue for SE-QCL DFB laser to improve the emitting efficiency while at the same time maintain an acceptable level of threshold gain. The effect of the thickness of every waveguide layer on the device performance is numerically investigated. Here we list the table for both real and imaginary part of materials parameters used in this modeling. These values are obtained from a Drude-Lorentz model:

$$(n-ik)^2=\varepsilon_\infty[1-\frac{\omega_p^2}{\omega_\eta^2}(1+\frac{i}{\omega\tau})], \tag{3.2-1}$$

where n and k are the real and imaginary parts of the refractive index; τ is the electron scattering time evaluated by the electron mobility μ_e and the effective electron mass m_e as $\tau=\mu_e m_e/e$ and $\eta=1+1/(\omega\tau)^2$; ω_p is the plasma frequency, given by $\omega_p^2=Ne^2/m_e\varepsilon_\infty\varepsilon$, where N is the concentration and ε_∞ is the high-frequency lattice dielectric constant.

Overall structure of SE-QCL has three layers of cladding with different doping concentrations of InP. Below cladding layers is active region, surrounded by InGaAs layer. Substrates are also made up by three InP layers with relatively low doping concentrations. Above the cladding layers is the grating part. For now it is set as straight square shape. Later we will discuss about different shapes influences. The grating consists of a metal (Au)/semiconductor

designed for different surface emission. Above the top and below the bottom part of the device is the interaction with air. The cross section view of SE-QCL device is attached here.

Table 3.2-1 Values of Material Parameters

Material	Doping	n	k	Epsilon_real	Epsilon_imag
InP	2.00E+16	3.099231	0.000019	9.605233	0.000118
InP	1.00E+17	3.096155	0.000094	9.586176	0.000582
InP	4.00E+17	3.08459	0.000377	9.514695	0.002326
InP	5.00E+18	2.901503	0.00501	8.481695	0.029073
InP	2.00E+19	2.201245	0.026417	4.844782	0.116301
Au	N/A	3.29885	28.250	-787.180	186.385
Ti	N/A	2.690708	8.051914	-57.7854	43.12116
RaZ 4.6 core	N/A	3.285356	2.53E-05	10.79357	0.000166
InGaAs	3.00E+16	3.410101	0.000047	11.62879	0.000321

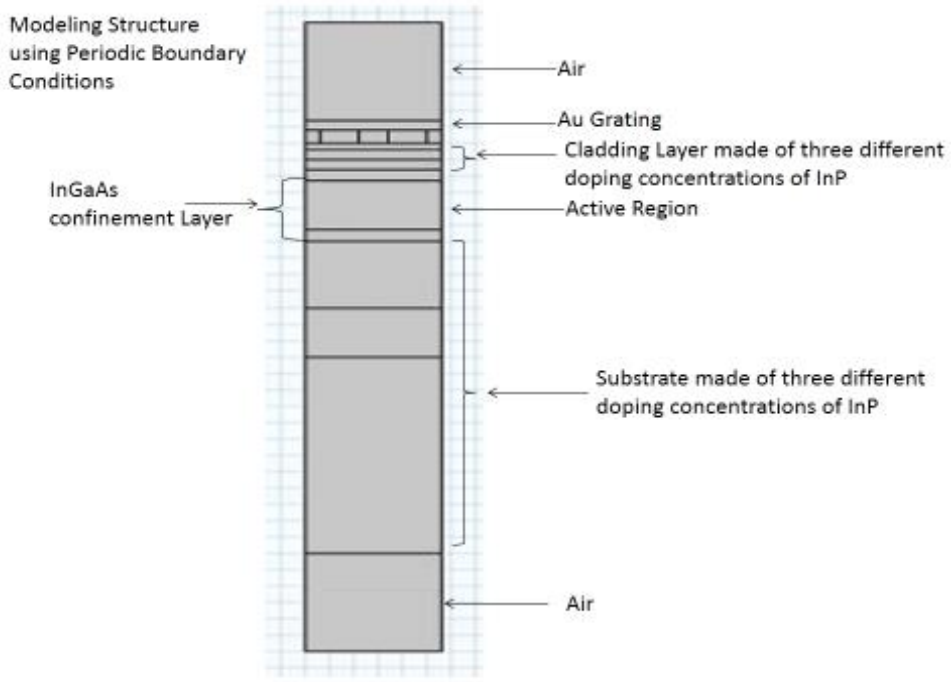

Figure 3.2-1 Two-dimensional Structure of SE-QCL Device Modeling

In COMSOL Multiphysics, setting up simulation environment is a key point, such as boundary conditions, solver configurations and meshing methods. For the initial running the simulation, it is assumed that the device is an infinite one which means that the boundary condition is periodic. In this case, it is easy to resolve the boundary problem between inside and

outside edge of device. For the solver setting, there are two common types of solvers: eigenfrequency and eigenvalue. The differences lie in that solution data set stores the solutions based on lambda (eigenvalue) or frequency (eigenfrequency). In SE-QCL modeling, eigenfrequency is chosen.

3.2.2 Analysis of SE-QCL Theory

To inform about the waveguide and grating design, we need to have a basic review of DFB grating properties. DFB grating has a periodic variation in refractive index that gives rise to a photonic gap around the Bragg frequency; the DFB supports lasing for longitudinal modes on either sides of the gap [16]. There are two modes that are directly at either edge of the photonic gap, which have the lowest lasing threshold of all the possible modes supported by the DFB [17]. We call them symmetric mode and anti-symmetric mode. The lower frequency one of the two modes is more concentrated in the higher index part of the grating, while the higher one more close to lower model effective refractive index. The grating's coupling strength is a complex number κ, whose real part is proportional to the photonic gap and whose imaginary part corresponds to the difference in loss (or gain) of the two DFB mode across the gap.

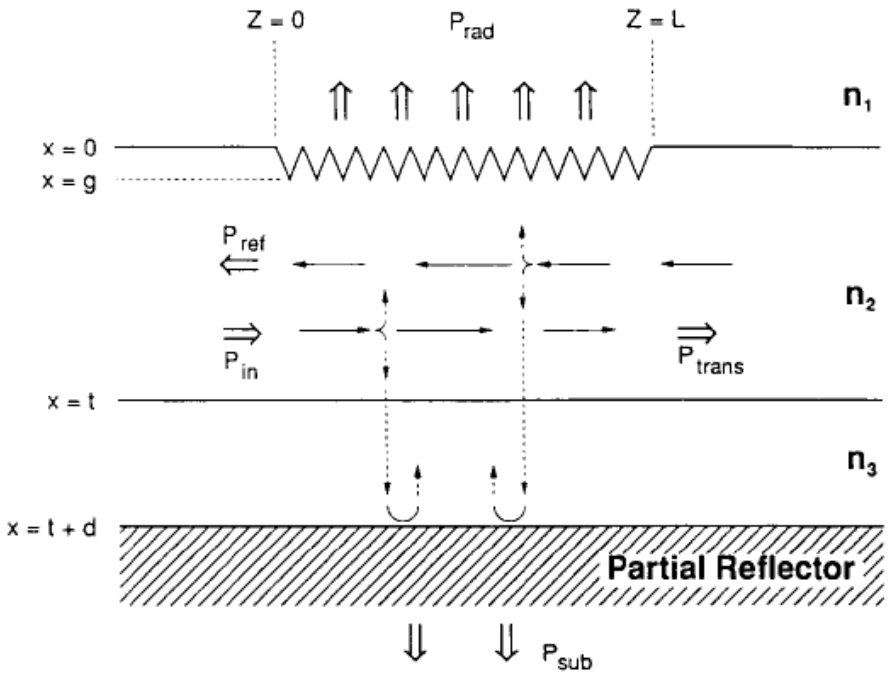

Figure 3.2-2 Illustration the Waveguide Grating Structure [18]

We analyze the situation based on Figure 3.2-2. A waveguide mode, incident from the left, has a complex amplitude at z=0. As the mode propagates along the waveguide it excites a counter-propagating mode. The interaction of these two modes is usually described by the coupled-mode theory, but for second and higher order gratings that theory is inaccurate. The lack of accuracy results from neglecting the interaction of the propagating modes with second-order grating to excite radiation and the reaction of the radiating fields on the propagating modes. In addition there are a set of non-radiating waves, which are excited by the guided modes such that the totality of all the waves satisfy the boundary conditions at the grating teeth. The inclusion of the dominant partial waves adds to the accuracy of the solution [19].

Propagating mode solutions for an infinite-length periodic grating structure can be found numerically as the Floquet-Bloch eigenmodes. When the propagation wavevector $2\pi n_{eff} / \lambda_0$ equals the Bragg wavevector $2\pi / \Lambda$, the mode is in resonance with the grating and two standing

wave solution exist, each at two slightly different frequencies, thus forming a bandgap at resonance [18]. This is analogous to the energy splitting at Brillouin-zone boundary for electronic dispersion in a periodic lattice. For propagation vectors close to $2\pi / \Lambda$, the modes of a finite-length DFB structure could be written as a linear superposition of the two resonant bandedge modes of the infinite-length grating, each multiplied by a slow-varying envelopes along the length of the grating [20]. This is a good approximation so long as the envelopes do not change rapidly over a distance of Λ. This approximation will, however, break down for small cavities or for slightly localized modes that can exist for some specific boundary conditions.

3.2.3 Confinement Factor and Radiation Loss

It is necessary to introduce optical confinement and radiation loss for analysis of SE-QCL device. The optical confinement factor Γ, which is defined as the fraction of the squared electric field confined to the active region, is an important parameter in calculating threshold current for semiconductor lasers and designing polarization insensitive semiconductor laser amplifiers [21]. In a slab waveguide with plates parallel to the y-z plane, the standard definition of Γ for a wave propagating along the z axis is the ratio of z-component power flow in the active region to the total power flow. The results are the ratio of the integral of $\left|E_y(x)\right|^2$ ($\left|H_y(x)\right|^2 / n_r^2$) over the active region to that over the whole cross section for TE (TM) modes, where n_r is the refractive index. The optical confinement factor defined as the proportion of the square of the electric field in the active region is also used in the analysis of VCSELs. In the analysis of semiconductor lasers, it is usually calculated the mode gain based on the optical confinement factor determined by the standard definition, which is in this SE-QCL modeling, based on the relation between the mode gain and the material gain.

To numerically investigate the influence of the device parameters, such as the grating duty cycle and the device length L on the device performance, it is necessary to analyze the infinite length device structure first. The period of the second-order grating is $\Lambda = 1.4163 \mu m$ with the effective index $n_{eff} = 3.2479$. In the symmetric eigenmodes, both positive and negative lobes appear between the teeth of the grating. This causes destructive interference outside the grating and consequently the anti-symmetric eigenmodes does not radiate. For the symmetric eigenmodes, only positive lobes appear. There is no interference, and the radiating component is non-zero. Therefore, there is higher loss in the symmetric eigenmodes due to the introduction of the surface radiation loss.

3.3 Simulation Results and Discussions

3.3.1 Two-dimensional Model Boundary Condition Settings

This section illustrates the results based on periodic boundary condition based SE-QCL device modeling, including mode profile, confinement factor, total loss and radiation loss and far-field plot. The first step is to give detailed values of dimensions of this two-dimensional structure of SE-QCL device. Figure 3.2-1 shows clearly the material arrangement, while here lists all thickness of this structure.

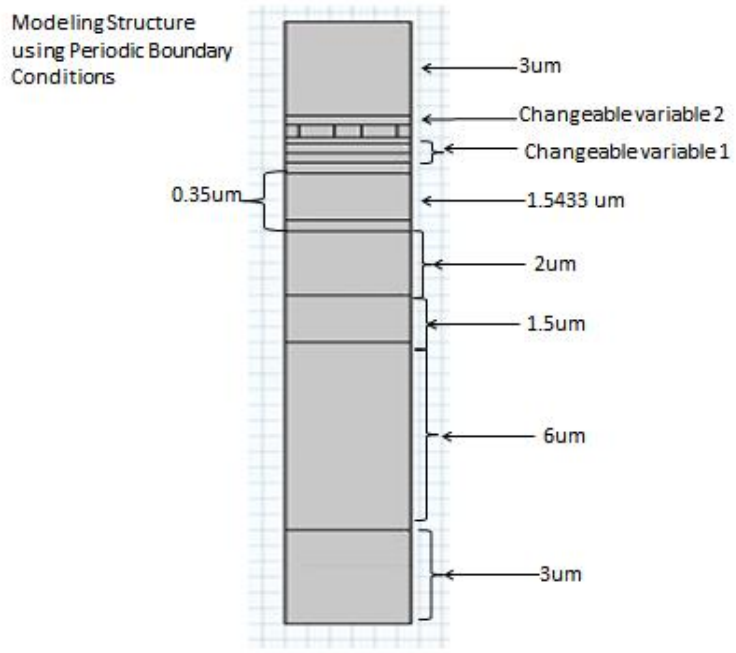

Figure 3.3-1 Detailed Values of Structure in Figure 3.2-1

A suitable boundary condition needs to be applied here. For static and quasi-static models, it is often possible to assume zero fields at the open boundary, provided that this is at a sufficient distance away from the sources. For radiation problems, special low-reflecting boundary conditions need to be applied. In many scattering and antenna-modeling problems, the outgoing radiation cannot be described as a plane wave with a well-known direction of propagation or as a

known, finite model expansion. In such situations, consider using perfectly matched layers (PMLs) would be a good choice. A PML is not, strictly speaking, a boundary condition but an additional domain that absorbs the incident radiation without producing reflections. It provides good performance for a wide range of incidence angles and is not particularly sensitive to the shape of the wave fronts. The PML formulation can be deduced from Maxwell's equations by introducing a complex-valued coordinate transformation under the additional requirement that the wave impedance should remain unaffected.

For the whole structure, because we are working on infinite-length case first, periodic boundary conditions (PBCs) can identify simple mappings on plane source and destination boundaries of equal shape. The destination can also be rotated with respect to the source. The specified type PBC chosen here is continuity which the tiny component of the solutions variable are equal on the source and destination. When dealing with radiation loss, there is another task about choosing scattering boundary conditions (SBCs). The scattering boundary condition is a first order absorbing boundary condition for a plane wave or a cylindrical or spherical wave, whereas a port boundary condition is a perfectly absorbing condition for general modes of a known shape, provided that the correct mode shape and propagation constant are supplied.

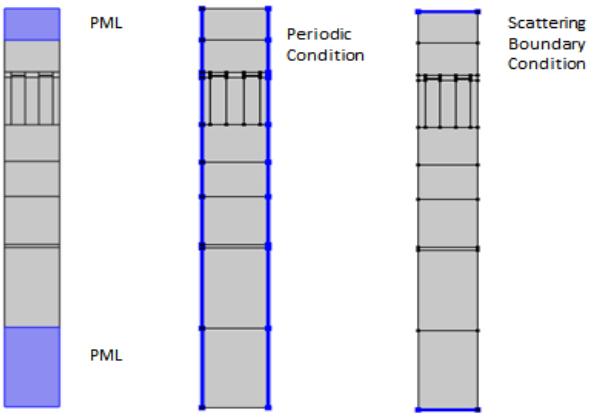

Figure 3.3-2 Boundary Conditions Setting for SE-QCL Modeling

3.3.2 Modes Profile and Confinement Factor

After setting up boundary conditions, materials and solver for modeling, it is about to start. First thing for processing the results is to find the symmetric and anti-symmetric mode. Both symmetric and anti-symmetric modes' frequency are around 6.55E+13. The three layers of cladding thickness (changeable variable 1) is set at around altogether 0.6 μm at this time, with a distribution of 0.24 μm, 0.16 μm and 0.2 μm separately. The grating thickness (changeable variable 2) is set at around 0.5 μm to guarantee that nearly no light would transmit through the metal part. Here are the plots for symmetric and anti-symmetric modes. When the positive and negative peaks are both between grating teeth, that corresponding mode belongs to symmetric modes, while the peaks are located at the edge of teeth, they are anti-symmetric modes. When the positive peak-negative peak has a same periodicity as grating periodicity, those are second order longitudinal modes while the positive-negative peak is twice as grating periodicity, those modes are first order longitudinal modes. All modes are fundamental transverse modes because they have only one peak within transverse direction.

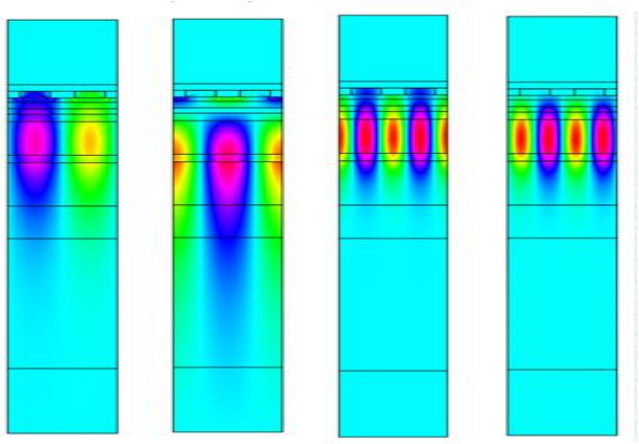

Figure 3.3-3 First and Second Order of Symmetric and Anti-symmetric Modes

The next step is to put the results about confinement factor (Γ). For discovering the influences of different cladding thickness, three different thickness (0.1 μm, 0.5 μm, 1.5 μm) has been tried. It is interesting to see when cladding thickness gets thinner or thicker, what would happen to Γ for both active region and grating.

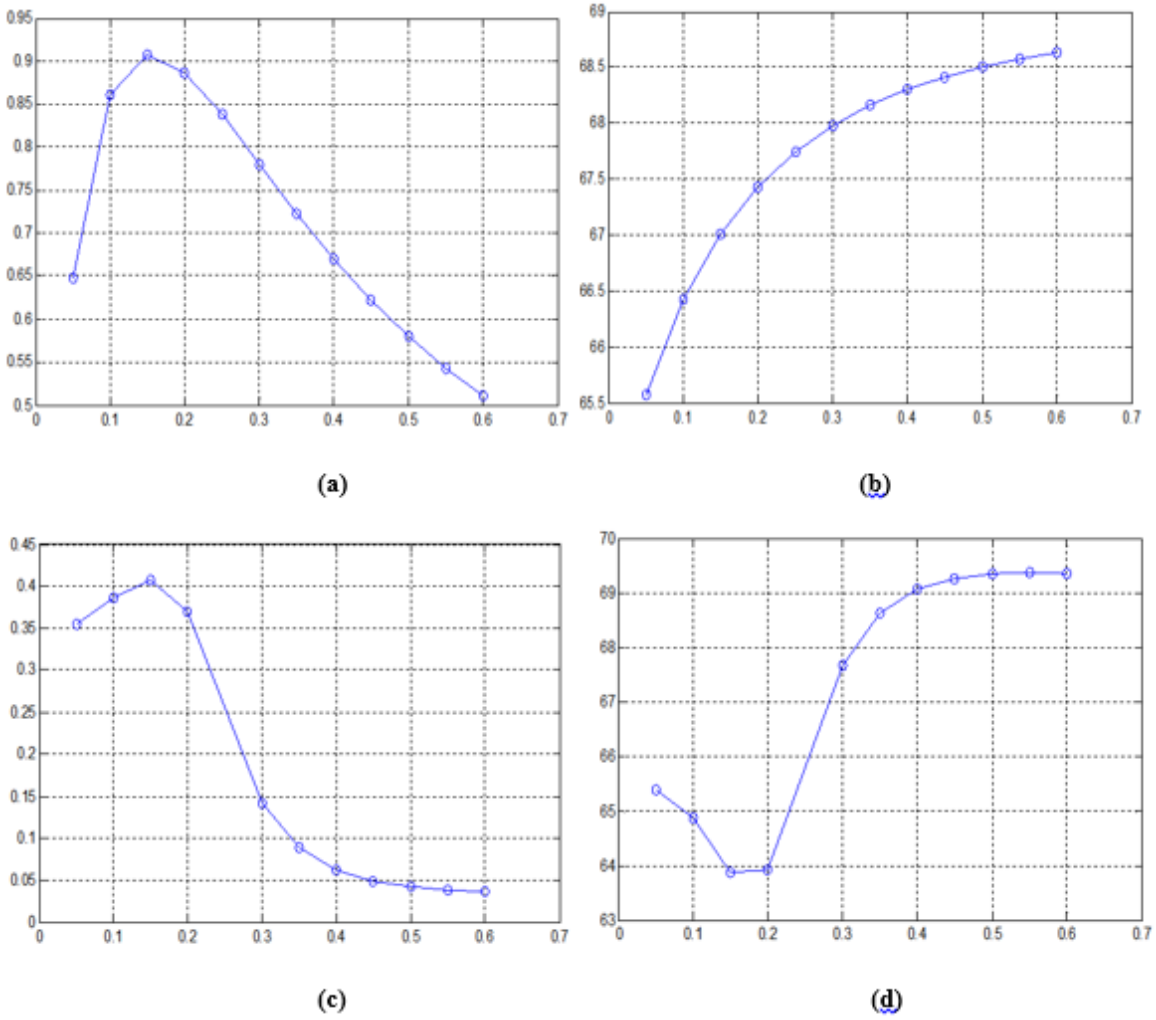

Figure 3.3-4 Optical Confinement Factor for 0.1 μm Cladding Thickness, both Symmetric and Anti-symmetric Modes, Active Region and Grating Part

Picture (a) is for symmetric mode grating part while (b) is for the active region. Plots (c) & (d) have same sequences but for both anti-symmetric modes. All plots y-axis are actually the Γ values in percentage. All plots x-axis are grating thickness in micron. Symmetric mode has a larger confinement factor than anti-symmetric mode in the grating part so that their radiation loss is much smaller for the anti-symmetric mode. An interesting phenomena is that Γ comes to a maximum point around 0.15 μm for both kinds of modes. This actually accords well with radiation loss which will be shown in next section. For the Γ within the grating part, another

interesting we found, is that, when cladding thickness increases to some larger values (0.5 μm), Γ achieves a maximum point, then the further the grating goes, the lower the Γ will be. This conclusion needs further study for a detailed explanation.

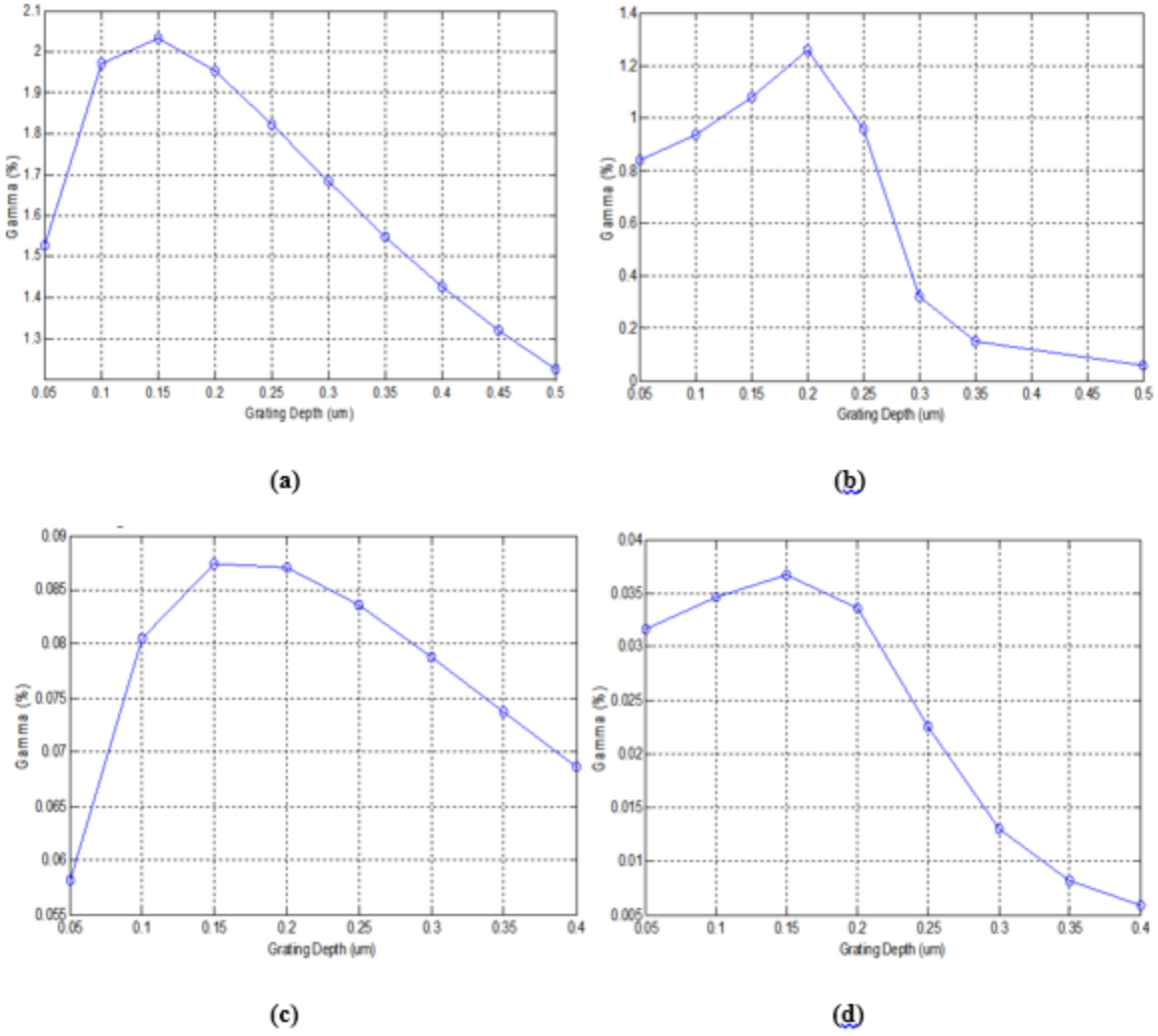

Figure 3.3-5 Γ for 0.5 and 1.5 μm Cladding Part, both Symmetric and Anti-symmetric Modes. (a) & (b) are 0.5 μm symmetric and anti-symmetric plots, (c) & (d) are 1.5 μm symmetric and anti-symmetric plots

3.3.3 Modal Loss and Radiation Loss

Modal loss for a semiconductor laser should contain radiation loss, absorption loss and some mirror loss. Because absorption loss is less than radiation loss in this picture, we want to investigate a method for calculation. As COMSOL Multiphysics will give modal loss only,

radiation loss can only approximated by some special settings. One possible method from previous experience is to set all imaginary part of semiconductor material zero while increasing imaginary part of metal 100 times more. The loss obtained from this method can roughly defined as radiation loss. The assumption needs to be demonstrated later by comparison. The cladding layer thickness is set 0.75 μm. The first plot below is modal loss and second one is radiation loss.

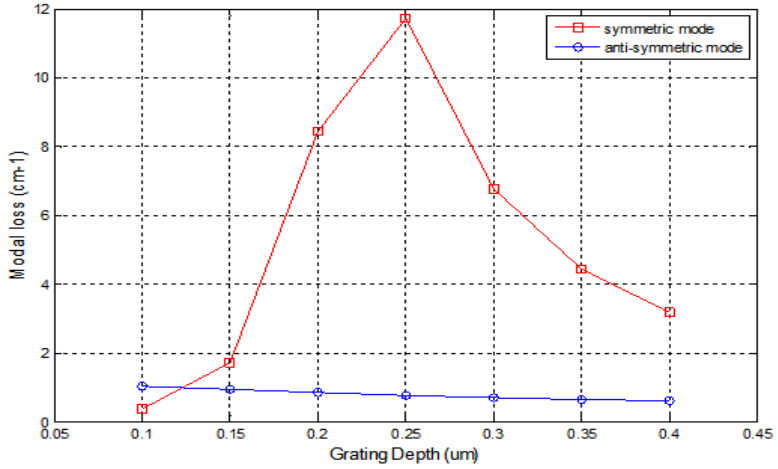

Figure 3.3-6 Modal Loss for 0.75 μm cladding layer thickness

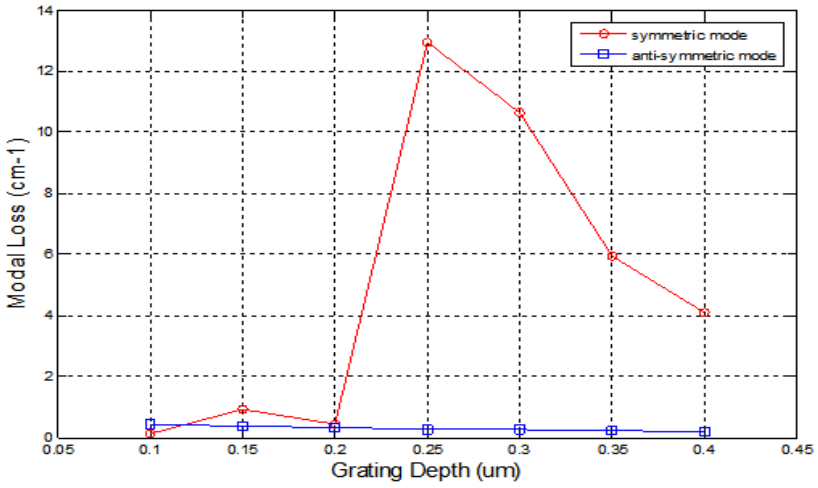

Figure 3.3-7 Radiation Loss for 0.75 μm Cladding Layer Thickness

There arises the problem, it is available to see that at grating depth 0.25 μm, radiation loss is larger than modal loss. This does not make sense because radiation loss should always be

smaller than modal loss. Another result is that anti-symmetric mode loss is much smaller than symmetric mode because in infinite case, anti-symmetric mode will not lase.

Above modeling is done by fixing cladding layer thickness at some value while at the same time changing grating depths. This actually induces a problem that the center of grating is increasing while the grating depth increases which is not a good way to observe the trend. So next simulation the center of active region to center of grating is fixed at different values, this means that as grating depth increases, cladding layers decreases. This will be better in analyzing effects from cladding layer side. Three different distances are chosen here: 2.02 μm, 2.47 μm and 3.17 μm for easy calculation. The curve obtained here has a peak point at roughly 0.45 μm, which needs further understanding.

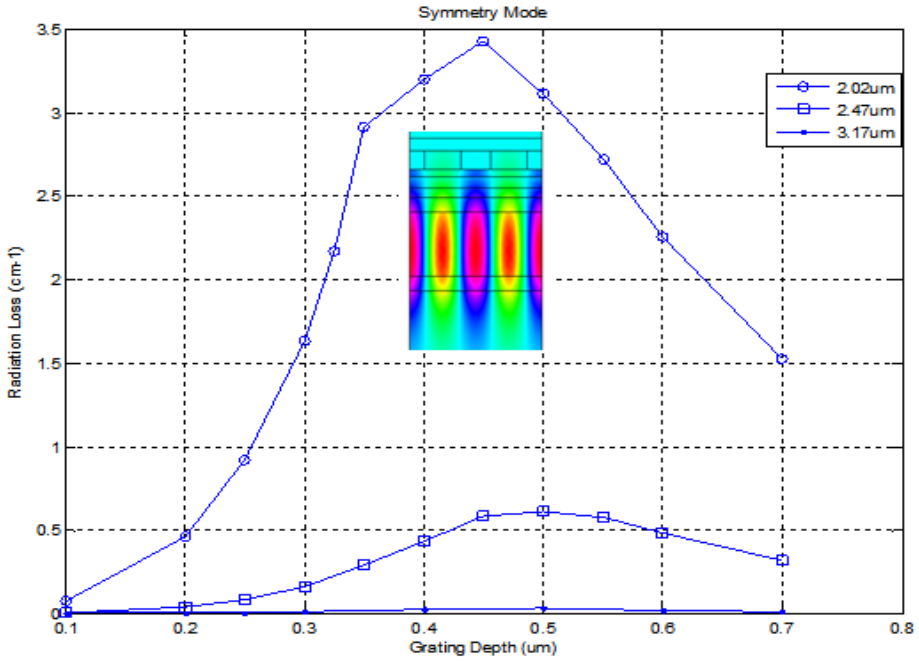

Figure 3.3-8 Radiation Loss for Different Cladding layer Thickness

3.4 Different Shape of Gratings

3.4.1 Methods for Waveguide Corrugations Calculations

Periodic corrugations are used in DFB and DBR lasers to provide the feedback mechanism for laser oscillation. In addition, these gratins are also employed as output couplers from laser and input couplers to dielectric thin-film waveguides. The important role that gratins fulfill have been a stimulus for many analytical studies of such periodic structure.

There are available a lot of analytical methods for calculating radiation and contra-directional mode coupling coefficients for waveguides with corrugations. For example, approximate explicit expressions of the radiation loss have been obtained for waveguides with a shallow sinusoidal corrugation profile. The exact solution for the guided waves in a corrugated waveguide with rectangular profile has been derived by Peng *et al*. In their method the periodic variation of the refractive index inside the corrugated region is expanded into a Fourier series. This together with the postulate that the wave solution for the structure can be represented as a sum of partial waves, lead to a set of coupled wave equations [22]. For a waveguide with a rectangular corrugation profile, the coefficients in the Fourier expansion of the refractive index in the corrugated region are constants, independent of the spatial coordinates. Thus, the coupled wave equations can be solved exactly, their solutions are in the form of exponentials. Alternatively, simpler, physically insightful perturbation methods may be employed to obtain less accurate but adequate solutions. Streifer *et al*. developed an iteration procedure based on perturbation solutions to obtained numerically exact solutions to coupled wave equations [23]. Corrugated waveguides with symmetrical triangular corrugation profiles and blazed grating have been also studied using the perturbation method.

Previous simulations are based on rectangular shape of grating, which is the easiest way to achieve in fabrication. Other types of gratings, include rectangular, sinusoidal and ladder-shape. Rectangular grating can be achieved by mask transfer and ladder-shape grating is actually more like a real state combining rectangular and ladder-shape. Sinusoidal grating is commonly studied in a lot of publications, because it has single Fourier spectrum, easy to analyze.

3.4.2 Sinusoidal, Triangular and Ladder-shape Grating Simulation Results

After revising the grating profile from rectangular to sinusoidal while keeping the same three distances from center of cladding to center of active region, results are available as below. The boundary of each periodicity is connected with each other, so there is no duty cycle discussion.

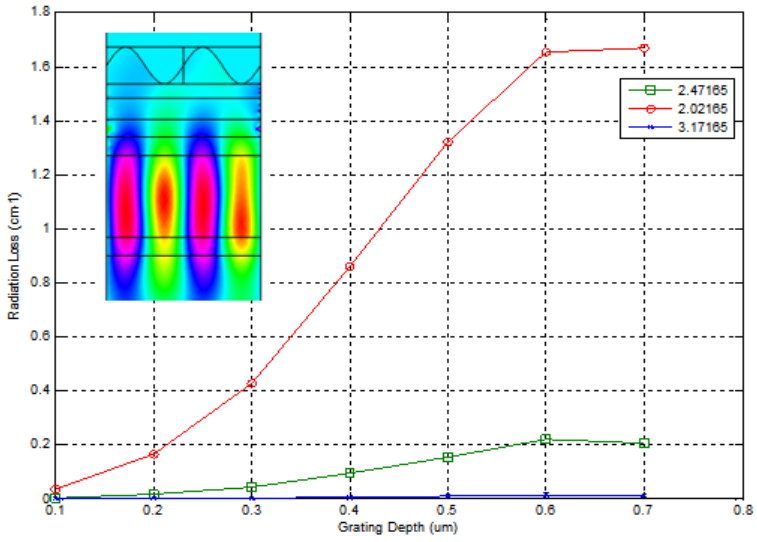

Figure 3.4-1 Sinusoidal Grating Radiation Loss versus Grating Depths

After sinusoidal, it is also available to put triangular gratings below. Here lists three duty cycle to see the influences how it affect. The duty cycle defined here is based on the base of semiconductor grating length versus base of metal grating length. So sinusoidal could be only

50:50, while triangular is off equal distribution. Another common definition of duty cycle is the distance of center semiconductor grating versus center of metal grating distance. In the simulation results, first definition of duty cycle is applied. It is interesting to research about duty cycle effects in the future, here only lists all simulation results and the conversion between two different duty cycles.

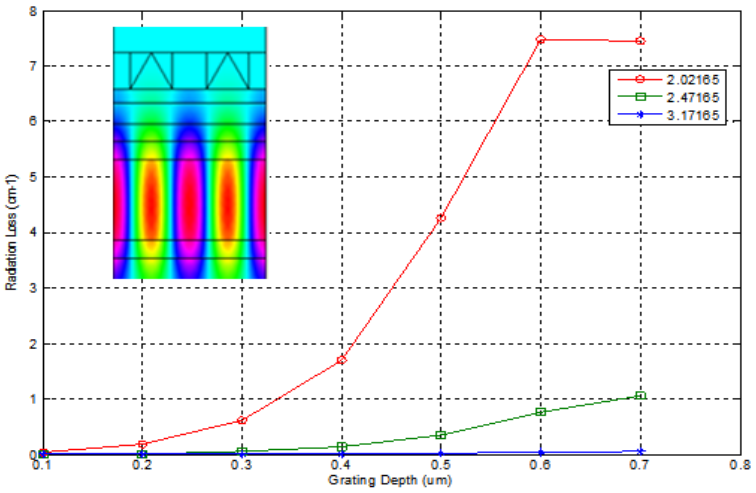

Figure 3.4-2 Triangular Grating Radiation Loss versus Grating Depths, with Duty Cycle 27.5:72.5

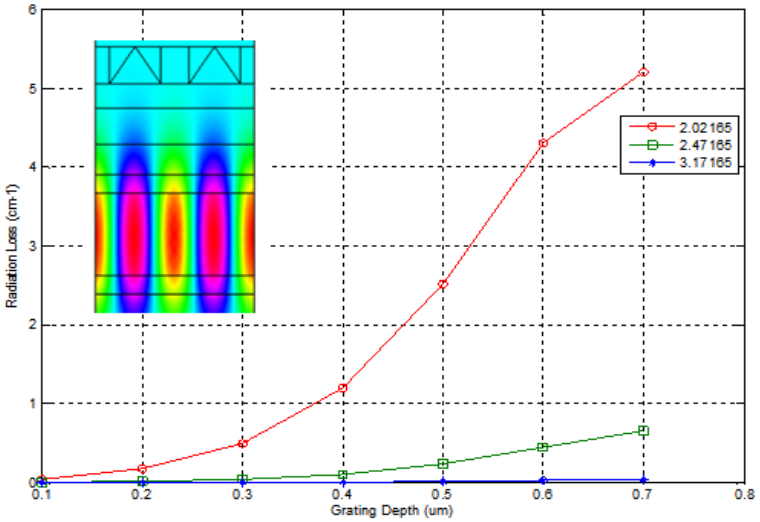

Figure 3.4-3 Triangular Grating Radiation Loss versus Grating Depths, with Duty Cycle 32.5:67.5

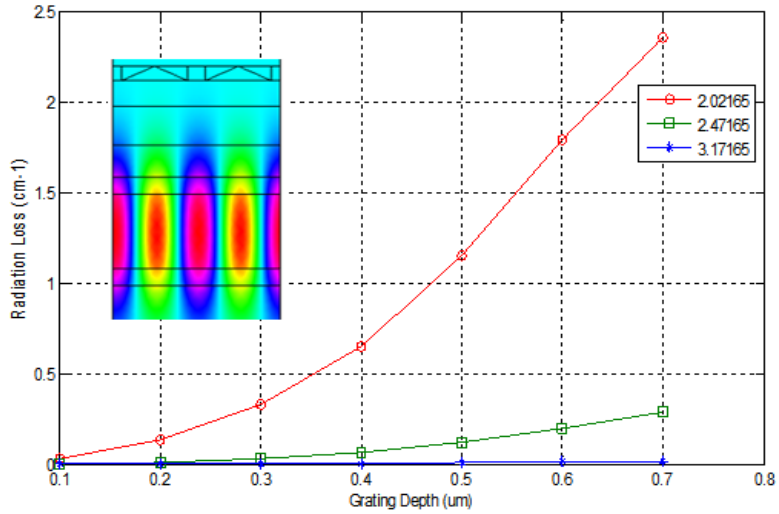

Figure 3.4-4 Triangular Grating Radiation Loss versus Grating Depths, with Duty Cycle 39.5:60.5

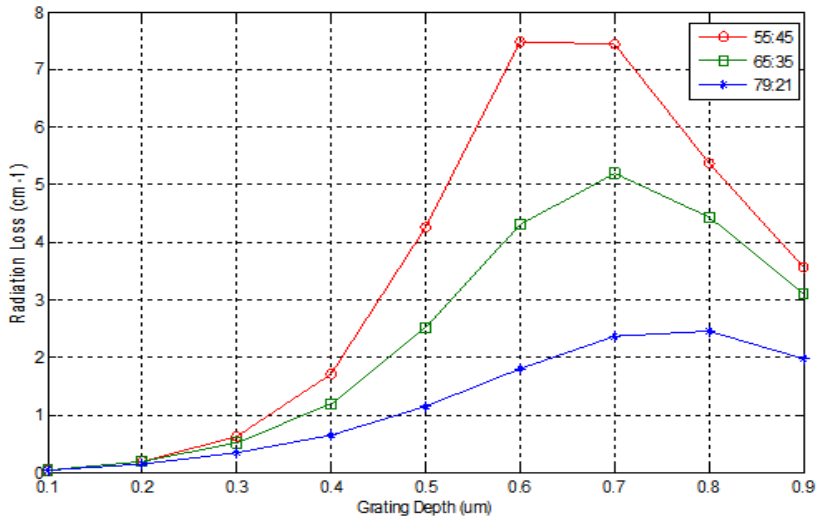

Figure 3.4-5 Summary of Different Duty Cycle Combinations

Table 3.4-1 Conversion between Two Duty Cycle Definitions

Definition 1	Definition 2
55:45	27.5:72.5
65:35	32.5:67.5
79:21	39.5:60.5

The ladder-shape is more like between triangular and rectangular gratings. There is also a duty cycle conversion problem here, but this time a little more complex. As the first definition of duty cycle is basis about bottom of semi/metal grating, when the grating depths gets more and more, the related duty cycle from second definition would be different because longitudinal widths of both semiconductor and metal are changing. So for each duty cycle ratio in the first definition, there is a separate form for different lengths. All the rest of settings are the same as before.

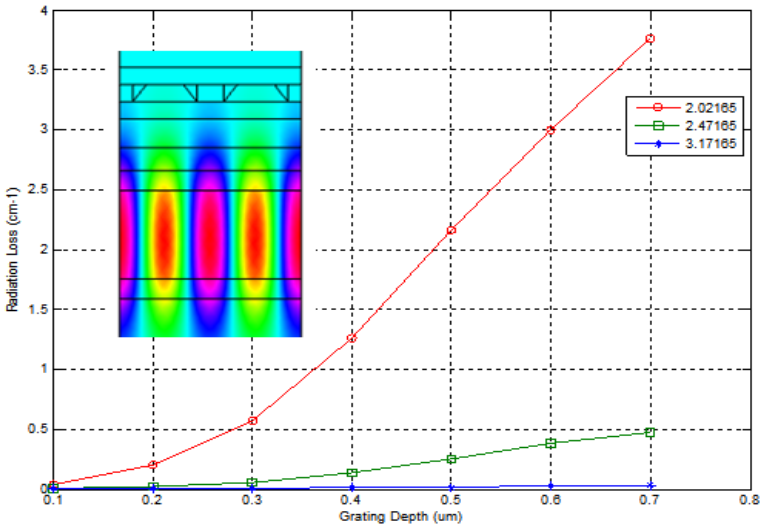

Figure 3.4-6 Ladder-shape Grating Radiation Loss versus Grating Depths, with Duty Cycle 79:21

Table 3.4-2 Duty Cycle under Different Grating Depths

Grating Depths (μm)	0.1	0.2	0.3	0.4	0.5	0.6	0.7
Duty Cycle	66:34	61:39	56:44	51:49	46:54	41:59	36:64

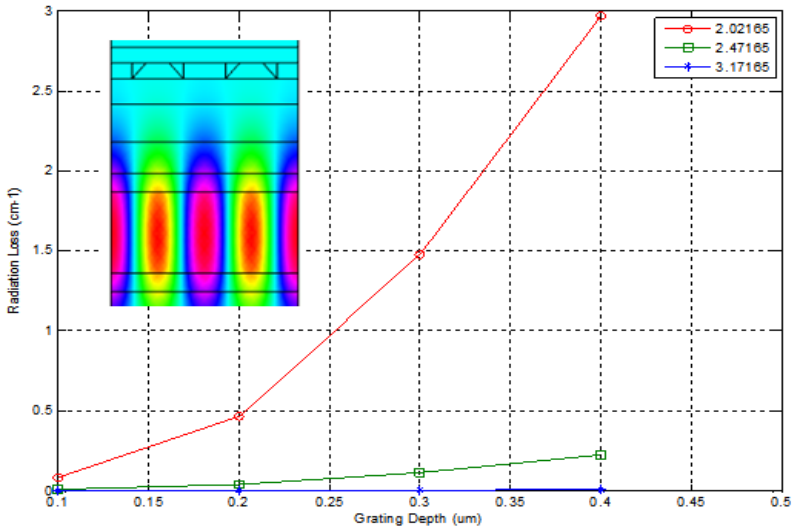

Figure 3.4-7 Ladder-shape Grating Radiation Loss versus Grating Depths, with Duty Cycle 55:45

Table 3.4-3 Duty Cycle under Different Grating Depth

Grating Depths (μm)	0.1	0.2	0.3	0.4	0.5	0.6	0.7
Related Duty Cycle 2	50:50	45:55	40:60	35:65	30:70	25:75	20:80

Here is the summary of all shapes of gratings, including rectangular ones discussed in last section. For the rectangular, sinusoidal and triangular, they all have a saturation point at some distance less than 0.9 μm. For the rectangular one, it is around 0.4 μm while for both sinusoidal and triangular are located around 0.6 to 0.7 μm. This phenomena right now is still under investigation, one thing needs to be taken care of is that within all modeling, the center of active region to center of grating is fixed, so all simulation results are based on a same distance from the center of active region. It would be very useful to extract the reason for the difference observed in the curves- in terms of radiation loss, i.e., why is the maximum point at somewhere between the thin and thick grating depth. Some surface plasmon resonance reason may be able to help explain this.

3.5 Conclusions

This chapter is the key part in this paper. SE-QCL is a hot topic in semiconductor laser research, and lots of publications have been issued from different sides in analysis. COMSOL Multiphysics has been playing as a major tool in analysis. Proper model constructions and settings are the most important part to make things working. Some interesting phenomena has been seen during simulations and for different types of grating part, ray optics is the probably the most direct way to explain. Far-field plot helped demonstrated the results and infinite-length is a good starting point for future research.

Future work on SE-QCL analysis could be π-phase shift application, thermal analysis for temperature profile and finite length modeling. For finite length, meshing is a tricky point because it would be better to have PML outside the model which will also increases the memory requirement. Some phenomena about surface plasmon resonance is also interesting to investigate.

Chapter 4
Description of Experiment and Results

This chapter documents the experimental set-ups and from preliminary experimental results, as preparation work for future implementation into the SEQCL device. Various microelectronic processing procedures are used for the device fabrication steps. SEM and AFM have been applied for taking etching and deposition images to calibrate etching rates and morphology. Finally, we come to a conclusion that ECR etching exhibits low surface roughness, although the ICP etching rate is faster and the results in a more stable process. Wet chemical etching may be used in a conjunction with a SiN_x hard-mask future experiment. Metal deposition on etched grating samples using Ti/Au show better adhesion than Au.

4.1 Sample Preparation and Etching Test

4.1.1 Wafer Preparation

The experiment sample is a 2-inch InP substrate wafer with a grating pattern defined by electron beam (e-beam) lithography. Top part of the wafer is a thin layer (a few microns) of highly doped InP with concentration 2E+19 cm^{-3}. The highly doped InP capping layer follows the design in Chapter 3. The e-beam lithography is performed at the University of Minnesota.

An illustration of top view of the grating design and layout on the wafer is shown in Fig. 4.1.1. "CleWin4" software is used for the grating layout design. The wafer is divided into are two halves, each with 3×5 stripe, as shown in Fig. 4.1.1. Each stripe is 2000 μm long and 100 μm width, with a grating period 1.42 μm.

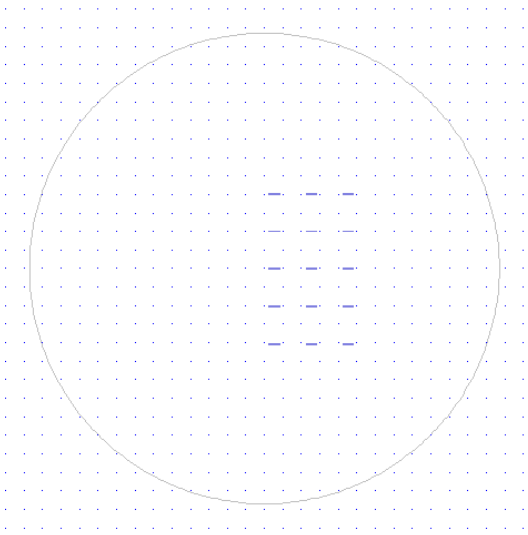

Figure 4.1-1 Lay-out of Wafer (designed by Chun-chieh Chang)

4.1.2 Etching Test

More about dimension description here and plus a plot from the software. PMMA stuff.

Figure 4.1-2 ICP, ECR and Metal Evaporation System (pictures taken from WCAM)

4.2 Inductively Coupled Plasma Etching

4.2.1 Working Mechanism

Inductively coupled plasma (ICP) is a type of plasma source produced by electromagnetic induction, that is, time-varying magnetic fields [24]. There are two types of ICP geometries: planar and cylindrical. In planar geometry, the electrode is a length of flat metal like a spiral (or coil). In cylindrical geometry, it is more like a helical spring. When a time-varying electric current is passed through the coil, it creates a time-varying magnetic field around it, which in turn induces azimuthal electric currents in the rarefied gas, leading to the formation of a plasma. In our experiment set-up, we use planar ICP etching, a system called 770 ICP Metal Etch system in Wisconsin Center for Applied Microelectronics (WCAM). Following the rules in WCAM, we choose recipe "GaAs10" for ICP etching.

Table 4.2-1 Recipe GaAs10 for ICP Etching on InP sample

Gas	Value on the Recipe	Actual Value in Experiment
Boron Trichloride 20	10	9.96
Argon 100	5.0	4.9

Initial test is based on a one-minute etching trial. Stable etching rate of approximately 225nm/minute is achieved. Since the designed grating depth is around 150nm, the etching time is decreased to 45 seconds. To record the results, pictures by optical microscope from a top view are taken.

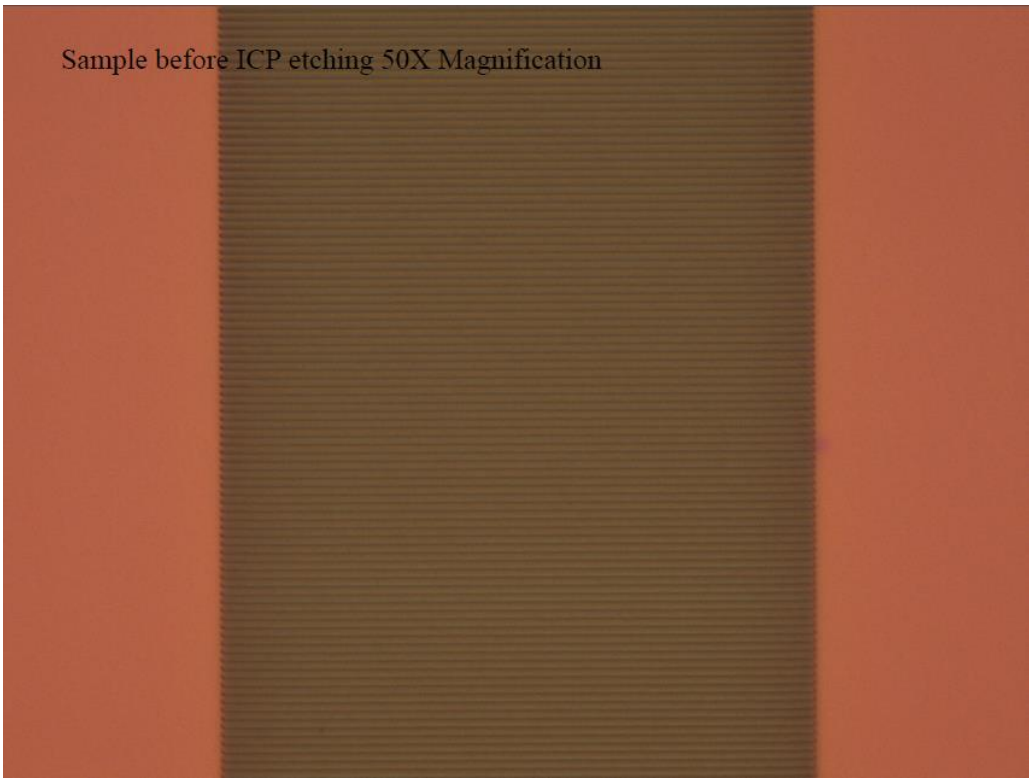

Figure 4.2-1 ICP Etching Pictures Taken from Optical Microscope before Etching

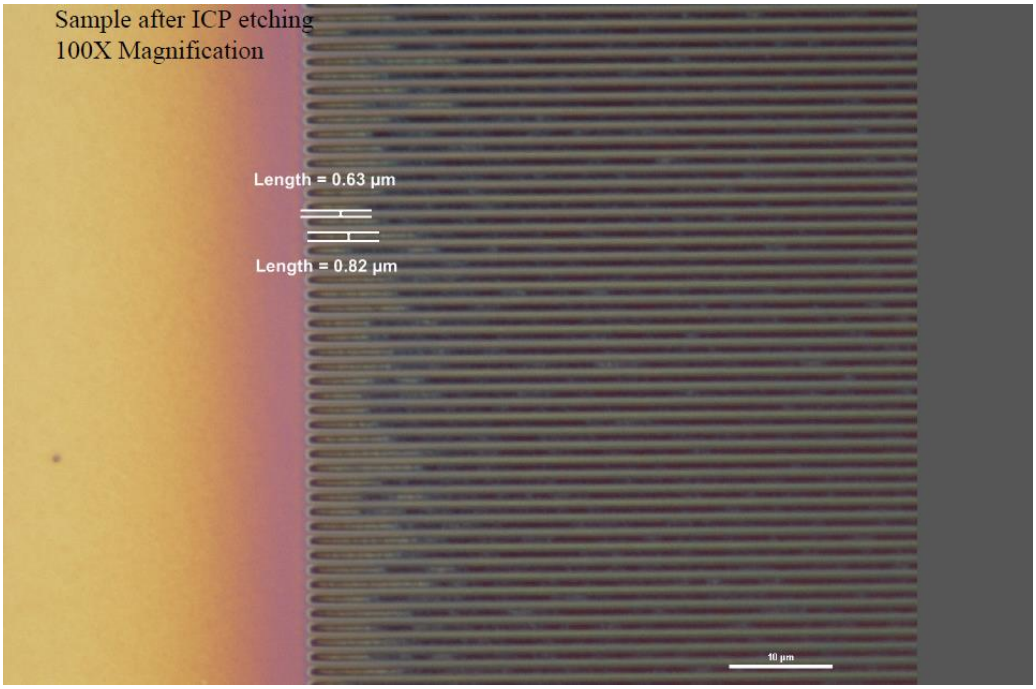

Figure 4.2-2 ICP Etching Pictures Taken from Optical Microscope after Etching

4.2.2 SEM Pictures of Etching Results

A scanning electron microscope (SEM) is a type of electron microscope used in research for obtaining images of a nanometer-scale sample. The working mechanism is by scanning the sample with a focused beam of electrons. The electrons interact with atoms in the sample, producing various signals that can be detected and contain information about the sample's surface topography and composition. The electron beam is generally scanned in a raster scan pattern, and the beam's position is combined with the detected signal to produce an image. Minimum feature such as 1nm can be reached by SEM.

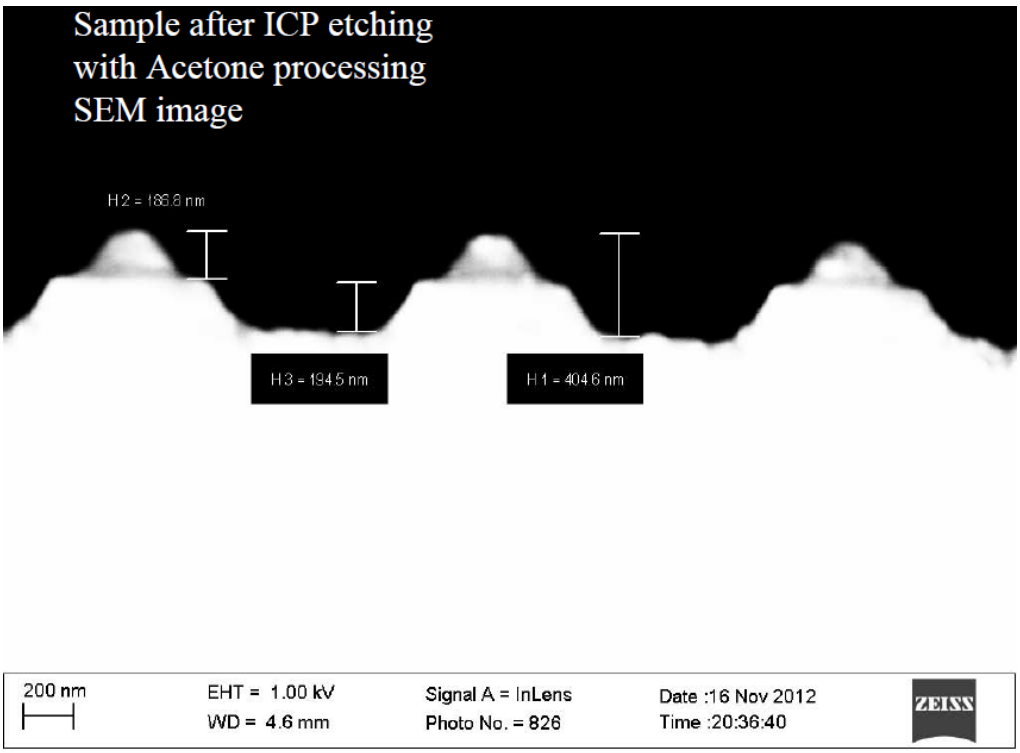

Figure 4.2-3 ICP Etching SEM Pictures, After Etching, with Acetone process

After etching, the sample is cleaved to observe the cross section of the grating. The cross-sectional SEM picture for ICP etching is shown above, in Fig. 4.2.3. The reason why sample after ICP etching has pyramid-like feature sitting on top of the grating is due to the left-over of

PMMA. It does not matter how to get an accurate etching rate here, but PMMA has to be removed before metal deposition. Acetone is first tried as removal, however, it is effective to photoresist AZ-5214 but not to polymer. Because of that, we put the etched sample in Reactive Ion Etching (RIE) chamber using Oxygen at power 150W for 10 minutes. It proves to totally get rid of PMMA after RIE. Eventually we get an estimate of ICP etching rate around 225 nm/min.

For another plasma etching mechanism electron cyclotron resonance (ECR) etching, we will introduce in next section and make a comparison based on their performances later.

4.3 Electron Cyclotron Resonance Etching

4.3.1 Working Mechanism

An electron in a static and uniform magnetic field will move in a circle due to the Lorentz force. The circular motion may be superimposed with a uniform axial motion, resulting in a helix, or with a uniform motion perpendicular to the field, for example, in the presence of an electrical or gravitational field, resulting in a cycloid. The angular frequency of this cyclotron motion for a given magnetic field strength B is given by electron charge multiplied by magnetic field over mass of electron. For the commonly used microwave frequency 2.45GHz and bare electron charge and mass, the resonance condition is met when B=0.0875T. For particles of charge q, rest mass m_0 moving at relativistic speeds, the formula needs to be adjusted according to the special theory of relativity to:

$$\omega = \frac{eB}{m} = \frac{qB}{\gamma \bullet m_0} \tag{4.3-1}$$

Where ω is angular frequency, B is magnetic field, q is the charge particles carry, γ is a coefficient based on special theory of relativity.

In plasma physics, ionized plasma may be efficiently produced by or heated by superimposing a static magnetic field and a high-frequency electromagnetic field at the electron cyclotron resonance frequency [25]. In the toroid magnetic field used in magnetic fusion energy research, the magnetic field decreases with the major radius, so the location of the power deposition can be controlled within about a centimeter. Furthermore, the heating power can be rapidly modulated and is deposited directly into the electrons. These properties make electron cyclotron heating a very valuable research tool for energy transport studies. In addition to

heating, electron cyclotron waves can be used to drive current. The inverse process of electron cyclotron emission can be used as a diagnostic of the radial electron temperature profile.

Table 4.3-1 Recipe InGaAsAl for ECR Etching on InP sample

Gas	Value on the Recipe	Actual Value in Experiment
Boron Trichloride 20	6.0	6.1
Argon 200	4.0	3.9
Hydrogen 100	8.0	7.7
Chlorine 100	4.0	3.9
Methane 100	5.0	4.7

4.3.2 Pictures of Etching Results

For ECR etching, the recipe "InGaAsAl" is chosen for calibration. Pictures from both optical microscope and SEM are listed here. PMMA is also left after on the grating. We use the same 150W RIE recipe to eliminate the PMMA.

Eventually a rate of 40-65 nm/min is obtained. Comparisons between two etching mechanisms will be carried out in next section, most of which is about the contrasts based on surface roughness, etching speed and stability between two mechanisms.

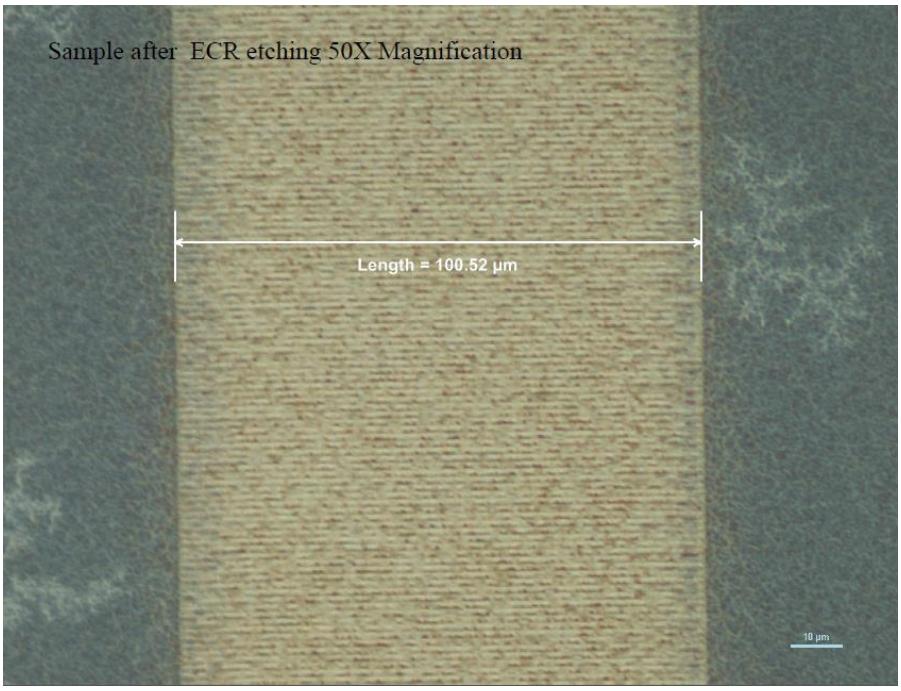

Figure 4.3-1 Pictures Taken from Optical Microscope before ECR Etching

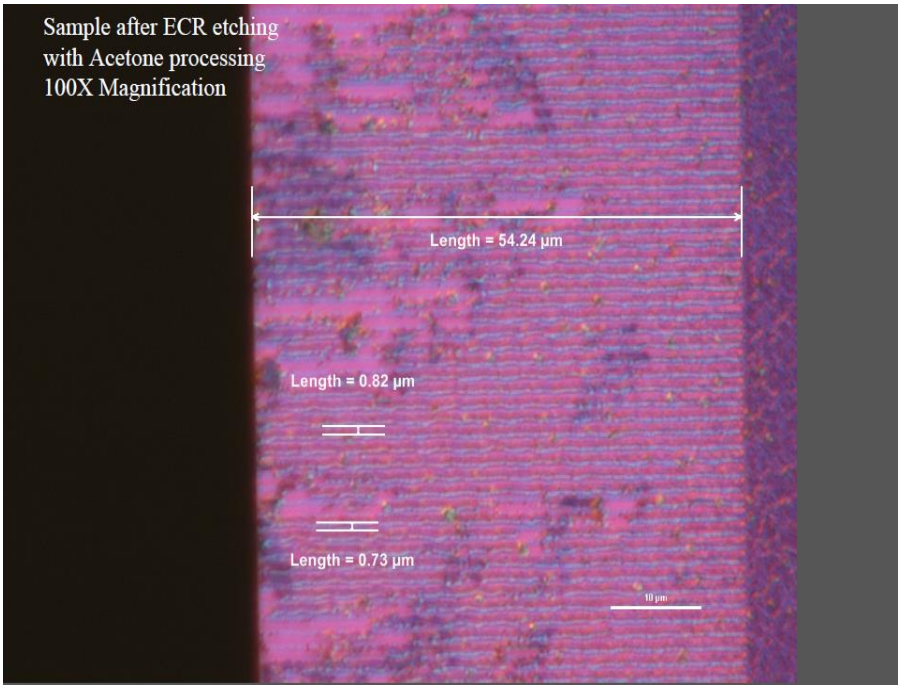

Figure 4.3-2 Pictures Taken from Optical Microscope after ECR Etching

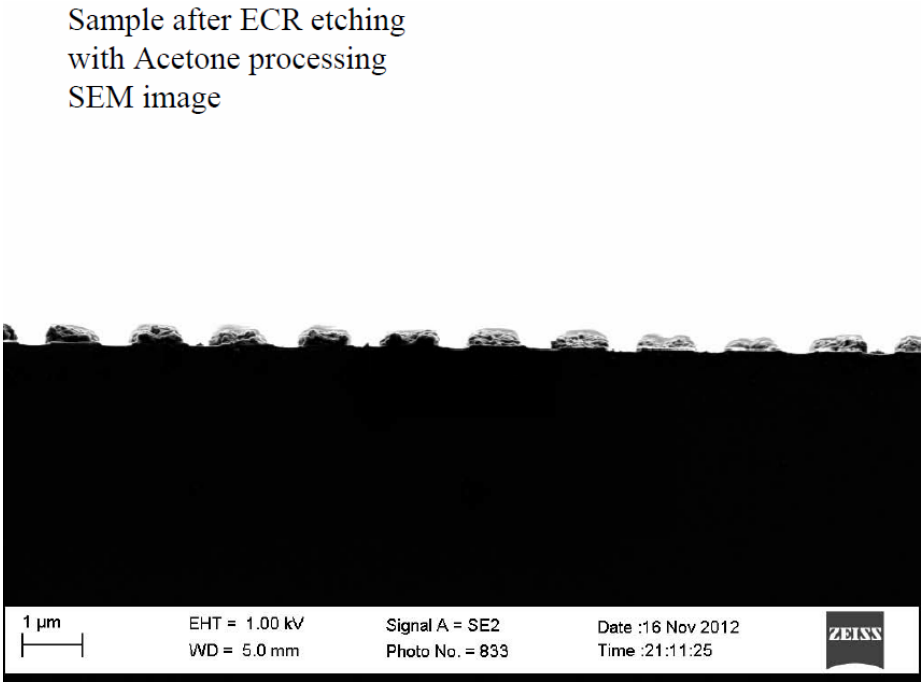

Figure 4.3-3 Pictures Taken from SEM after ECR Etching, with Acetone process

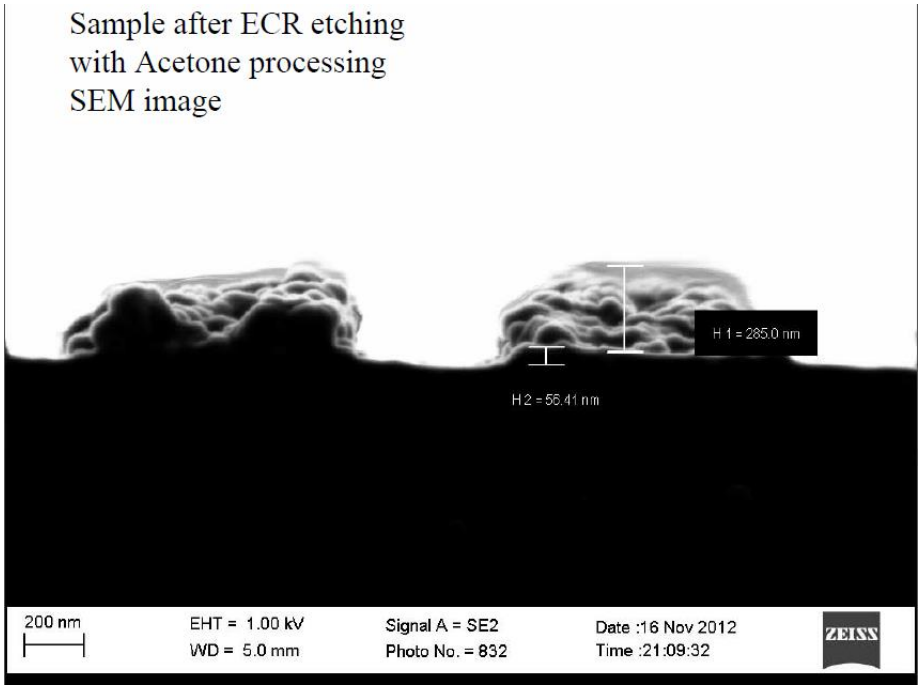

Figure 4.3-4 Detailed Pictures Taken from SEM after ECR Etching, with Acetone process

4.4 Comparison between Two Etching Mechanisms

4.4.1 Surface Roughness

For the purpose of surface roughness comparison, the Atomic Force Microscope (AFM) is introduced as major tool [26].

AFM is a very high-resolution type scanning probe microscopy, with demonstrated resolution on the order of fractions of a nanometer, more than 1000 times better than optical diffraction limit. Gerd Binning, Calvin Quate and Christoph Gerber invented the first AFM at IBM Research-Zurich, a development which earned them the Nobel Prize for Physics in 1986. The AFM consists of a cantilever with a sharp tip (probe) at its end that is used to scan the specimen surface. The information from AFM is gathered by feedback from the surface with the tip. When the tip is approaching the surface, forces between it and the sample lead to a deflection of the cantilever according to Hooke's law. Typically, the deflection is measured using a laser spot reflected from the top surface of the cantilever into an array of photodiodes. Piezoelectric elements that facilitate tiny but accurate and precise movements on command enable very precise scanning.

In SEQCL detection, tapping mode is chosen for best performance. In tapping mode, the cantilever is driven to oscillate up and down at near its resonance frequency in tip holder. The interaction of forces acting on the cantilever when the tip comes close to the surface causes the amplitude of this oscillation decrease as the tip gets closer to the sample. An electronic servo uses the piezoelectric actuator to control the height of the cantilever above the sample. The servo adjusts the height to maintain a set cantilever oscillation amplitude as the cantilever is scanned over the sample. A tapping AFM image is therefore produced by imaging the force of the

intermittent contacts of the tip with the sample surface. This method causes less damage to the sample than other modes, such as contact mode and non-contact mode.

Measurements are taken in Reed Center for Photonics at University of Wisconsin-Madison, by a Multimode Scanning Probe Microscopy system from Veeco Instrument Company. Extremely fine tip with working length 1-3nm for the best performance is applied.

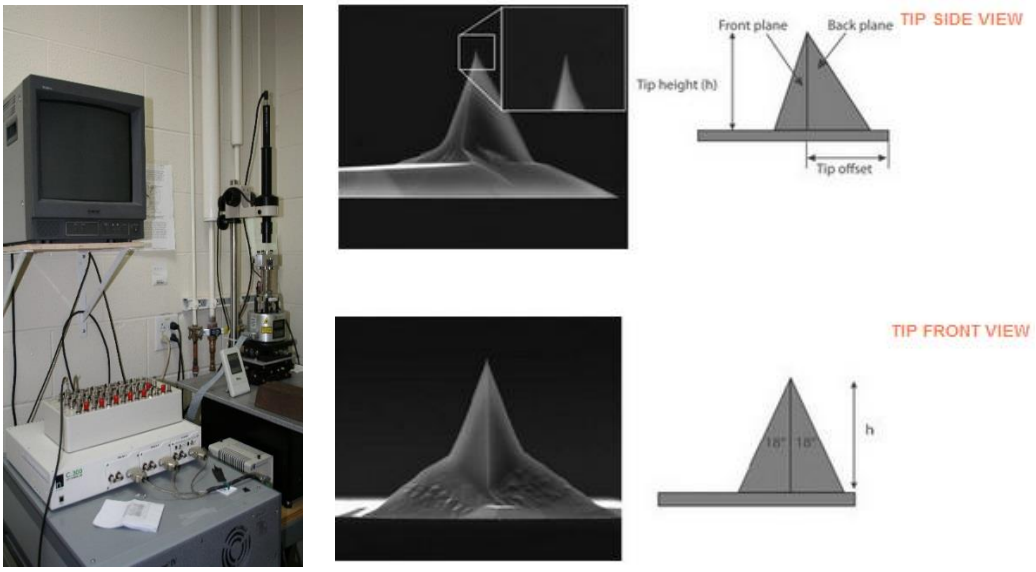

Figure 4.4-1 AFM System (picture taken from Material Science Center) and Cantilever Pictures

With AFM system and fine tips, it is possible to carry on the roughness comparison. First, a raw sample with 2E+19 cm^{-3} doping without any processing is scanned. This raw sample acts as a baseline sample. After that, careful work on small sample with gratings on it is done. Tricky point locates that as samples have been cut into halves by diamond scribe before so gratings are on the edge of scribed samples. So it needs very careful work to locate the laser spot and tip right above the grating, which takes time and patience. Below are some results from AFM system where the pictures have been processed by specified image processing software.

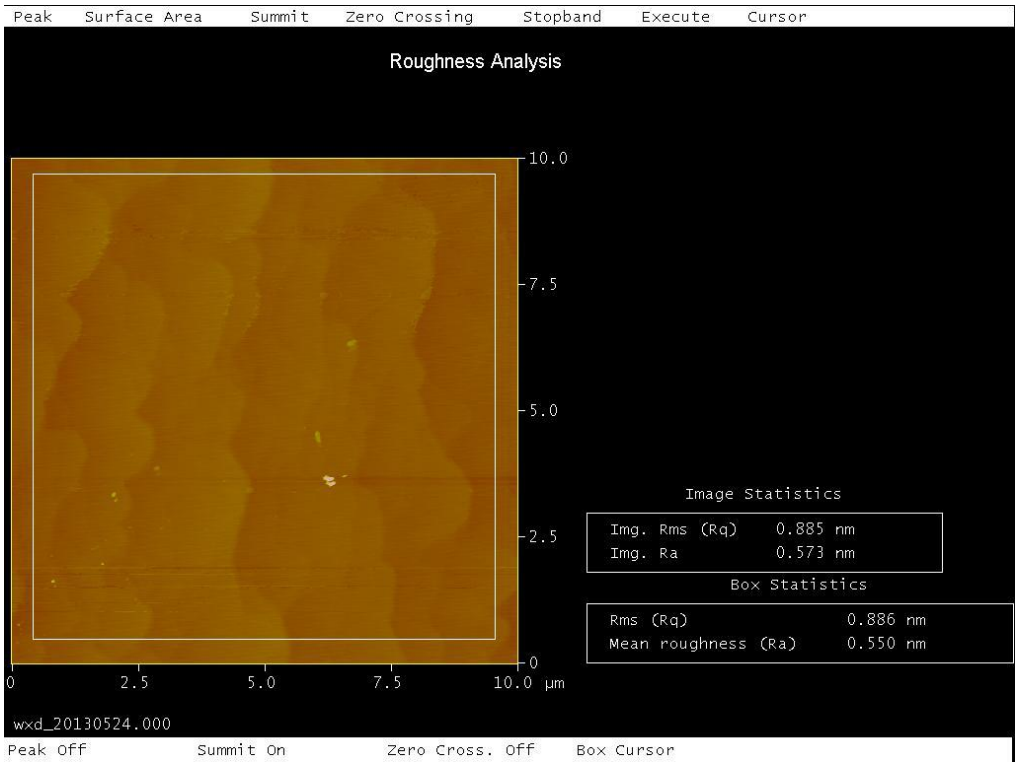

Figure 4.4-2 Raw Sample AFM Roughness Analysis Pictures

The first picture is from the raw sample, already processed from collected signal. It shows that as to highly doped InP sample, mean roughness is around 0.55nm while root mean square (RMS) for average is 0.886nm.

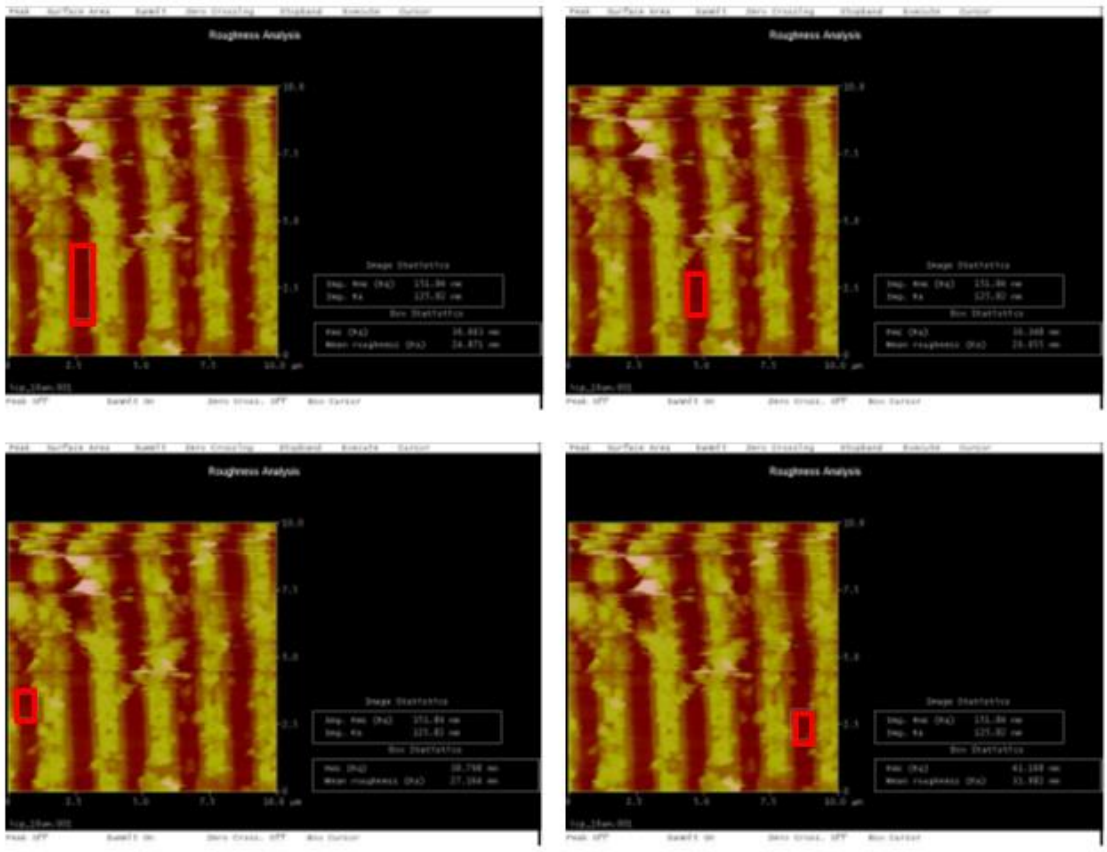

Figure 4.4-3 ICP Etching Sample AFM Roughness Analysis Pictures (four different areas)

From ICP sample etched 45 seconds, several parts from one single sample are scanned and four mean values obtained for roughness, 24.871nm, 20.055nm, 27.164nm and 31.982nm, separately. Corresponding RMS is 36.661nm, 30.348nm, 38.798nm and 41.168nm. Average mean value for roughness inside the grating is 26.018nm and average RMS is 36.744nm.

Table 4.4-1 : Mean Roughness and RMS Value for ICP Etching

Item	Measure 1	Measure 2	Measure 3	Measure 4	Average
Mean (nm)	24.871	20.055	27.164	31.982	26.018
RMS (nm)	36.661	30.348	38.798	41.168	36.744

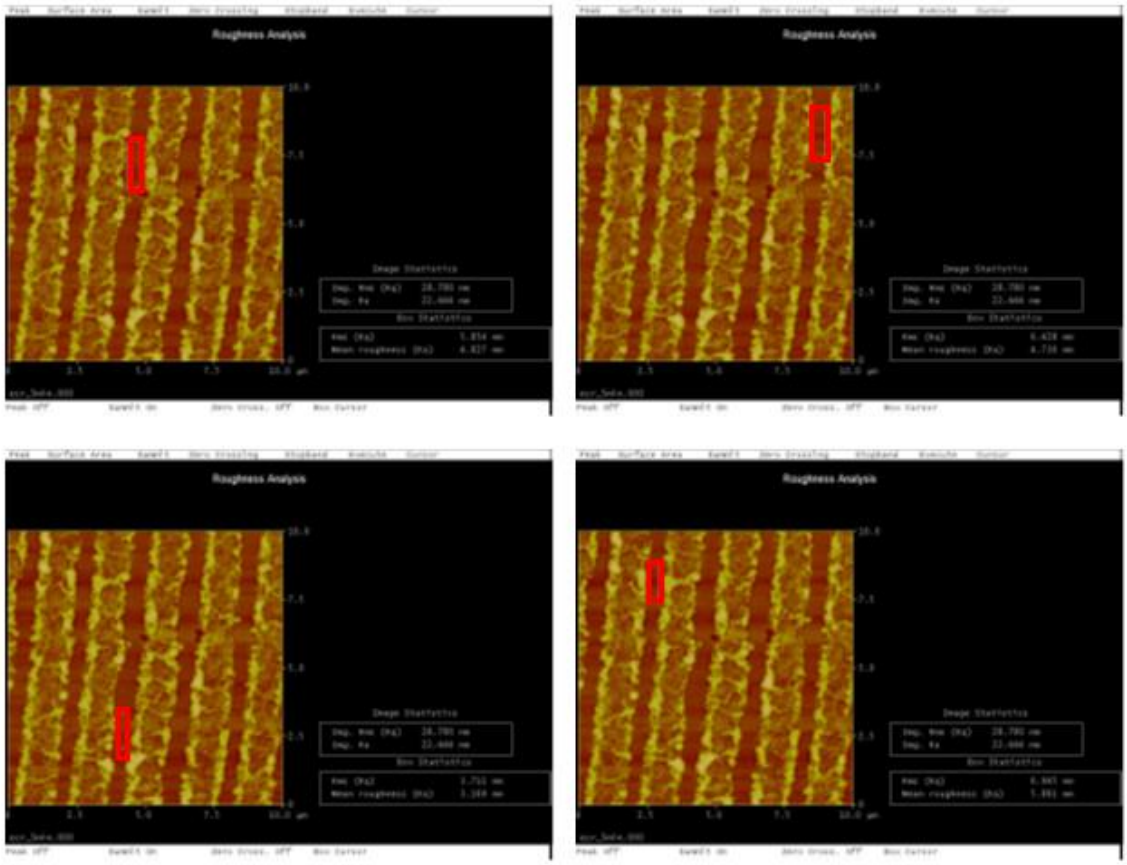

Figure 4.4-4 ECR Etching Sample AFM Roughness Analysis Pictures (four different areas)

ECR shows a much smaller mean roughness, average is around 4.65nm. Measured results are 4.827nm, 4.730nm, 3.169nm and 5.861nm. RMS is also smaller than previous, 5.854nm, 6.428nm, 3.711nm and 6.945nm, of all average is 5.74nm. It does indeed demonstrate ECR is better than ICP in surfaces smoothness.

Table 4.4-2 Mean Roughness and RMS Value for ECR Etching

Item	Measure 1	Measure 2	Measure 3	Measure 4	Average
Mean (nm)	4.827	4.730	3.169	5.861	4.647
RMS (nm)	5.854	6.428	3.711	6.945	5.735

4.4.2 Etching Rate and Stability

As introduced before, ICP etching rate is about 5 times larger than ECR etching (225nm/min and 50nm/min). In current design, grating depth aims at around 150-200nm. ECR showing a slower rate seems more easily to precisely control depth. The etching speed achieved depends a lot on experimental conditions. Besides, ECR etched surface is much flatter than ICP. This lessens the influences of coupling efficiency decrease by surface roughness.

However, from experience it has to point out that, ECR etching rate has more variation range in experiment. First reason is by loading effect. Due to environment pattern variations, isolated and dense patterns have different etching biases. Every time ECR etching is carried on, a highly doped InP wafer with a fixed size should be beneath the sample. In experiment, after once etching done, loading wafer would change its color, first blue, then darker to black. This loading wafer induces etching rate unstable. Sometimes it can even prevent etching from happening. That is why etching rate mentioned before is located within a range. It would an important issue in fabrication time.

4.5 Metal Deposition on Etched Samples

4.5.1 Working Mechanism

The system for metal deposition is an electron beam vapor evaporation. Evaporation is a common method of thin film deposition [27]. The source material is evaporated in a vacuum. The vacuum environment allows vapor particles to travel directly to target object, where they condense back to a solid state. Evaporation is used in micro-fabrication to make macro-scale products such metallized plastic film.

Evaporation involves two steps: a hot source material generates and condenses on the substrate. Evaporation happens within a high vacuum environment, enabling particles travelling a long pathway without colliding with background gas. Hot objects in chamber, for example, heating filaments, provide some unexpected vapors which will limit the quality of evaporation. Evaporated atoms the collide with background particles may have reaction with them, for example, if aluminum is deposited with in the presence of oxygen, aluminum oxide will be formed. Another important feature for evaporation is that evaporated materials will have non-uniformly surface if they have rough surfaces. Because evaporated materials attack the substrate from a single direction, protrude features block the evaporated from some areas, which is called "step coverage".

A simple comparison with other methods of deposition is summarized. Sputtering and chemical vapor depositions are also popular. They have better "step coverage" than evaporation. Sputtering has a slower deposition rate than evaporation, which uses plasma to produce high-speed atoms bombard the substrate. This will somewhat damage the substrate. From evaporation side, atoms follow a Maxwell distribution so high-speed atoms are limited in overall proportion.

However, electron beams may produce some X-rays and stray atoms, which may also damage the substrate somehow.

4.5.2 SEM pictures of Deposition Performances

As discussed in last section, there is roughness problem after plasma etching; especially for ICP etching, so first consideration is trying to smooth the surface. Reactive Ion Etching (RIE) is found to effectively eliminate PMMA after etching. This process is to guarantee that no other PMMA influences the rest of deposition. Fig. 4.5.1 is a SEM image for deposition 200 nm without any lift-off process and only Au is evaporated. It is obvious that deposition is not uniform on the surface. So we choose to optimized by the use of diluted HCl (HCL: H2O=1:3) as immersing liquid which has a relatively low etching rate around 20 nm/min to flatten the surface. We can ignore etching influences from acid due to very short immersed time (5 and 15 seconds).

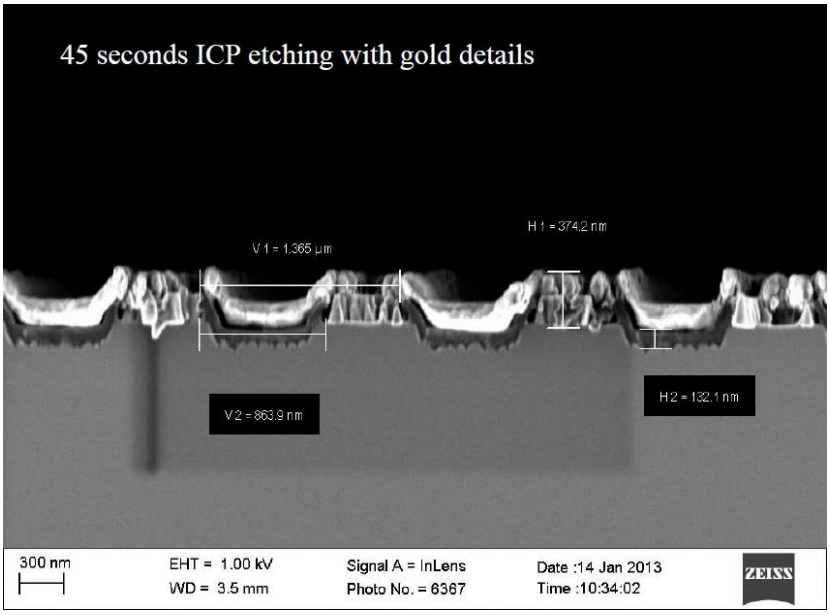

Figure 4.5-1 Pictures Taken from SEM after Deposition, without smooth process

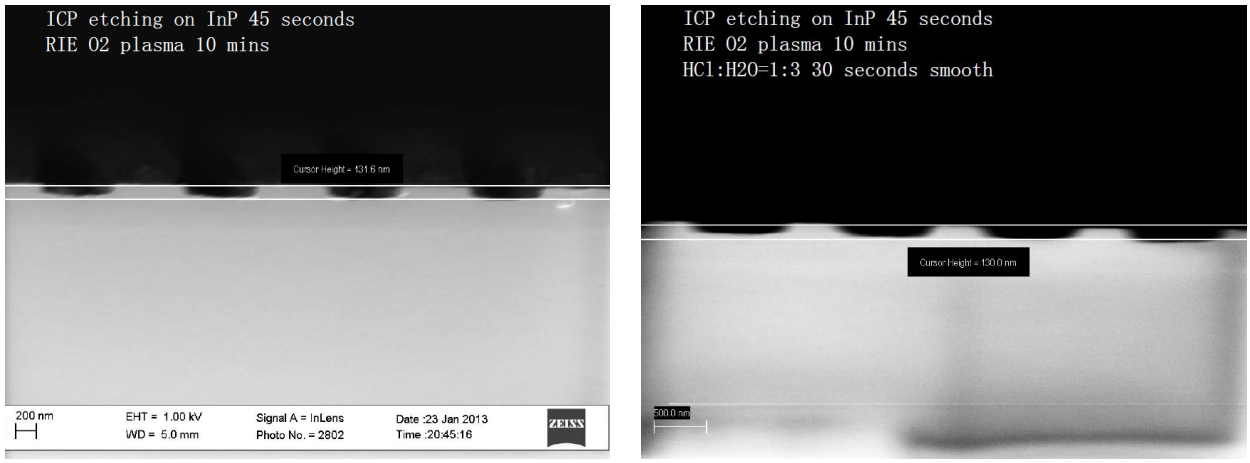

Figure 4.5-2 SEM Pictures with RIE Etching before Deposition, without and with smooth process

Another improvement comes from selection of evaporated materials. Ti can play an attaching role connecting gold to semiconductor. Before evaporated 200nm Au into the chamber, 20 nm Ti is used with a lower vacuum level (8E-8 Torr) than normal deposition vacuum requirement (2E-7 Torr) to prevent oxidation. Different time put in diluted HCl is also applied here for better comparison.

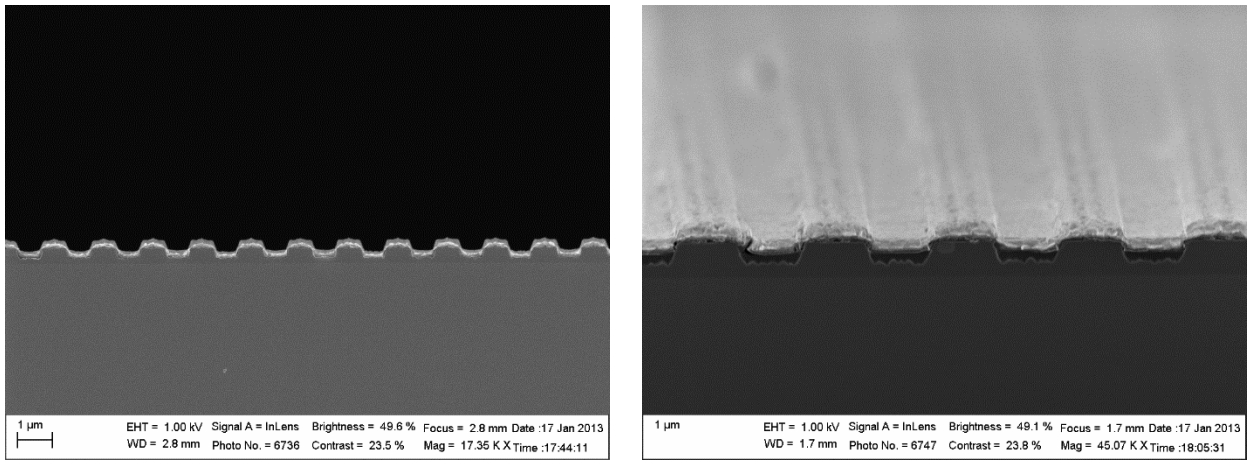

Figure 4.5-3 SEM Pictures without HCl Smoothness, Cross Section and 75 degree Size View

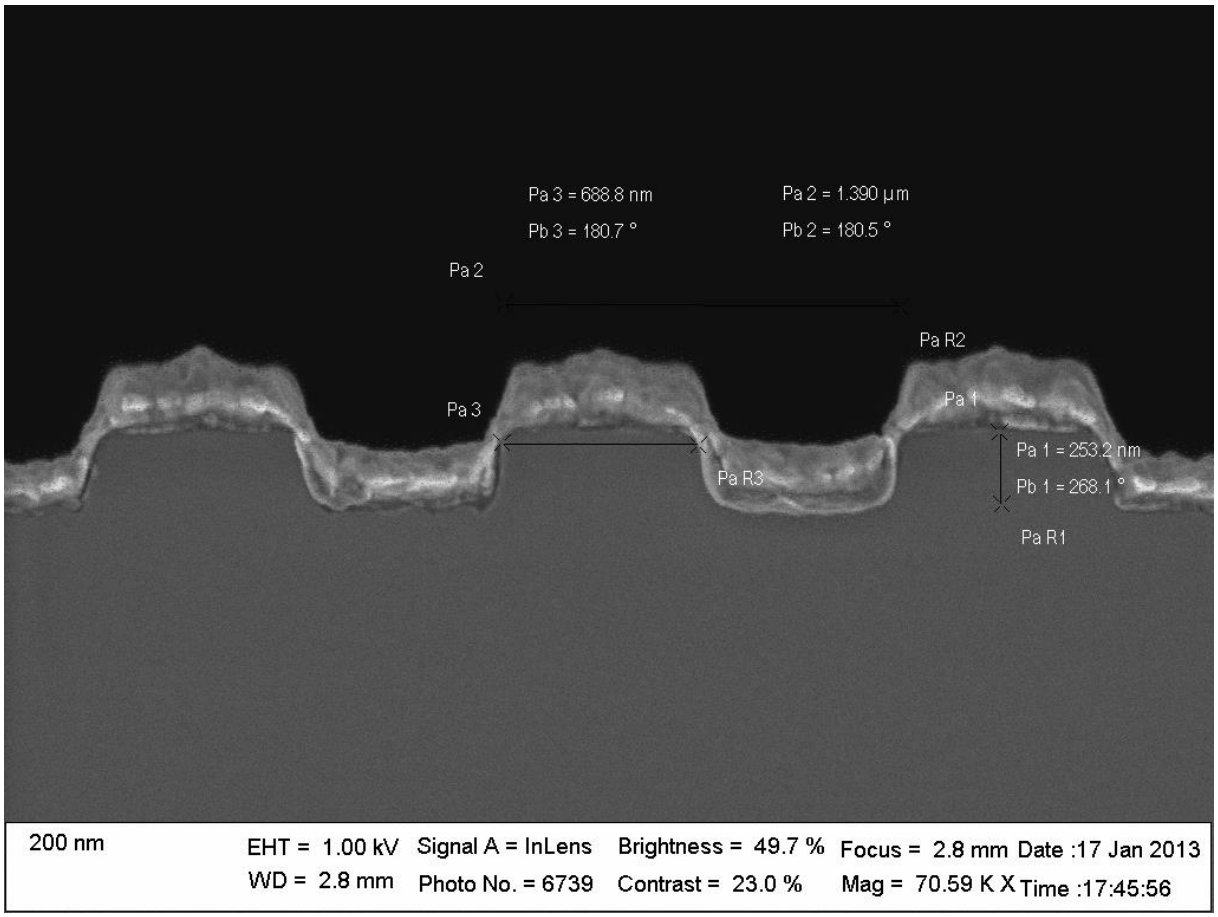

Figure 4.5-4 SEM Zoomed Pictures without HCl Smoothness

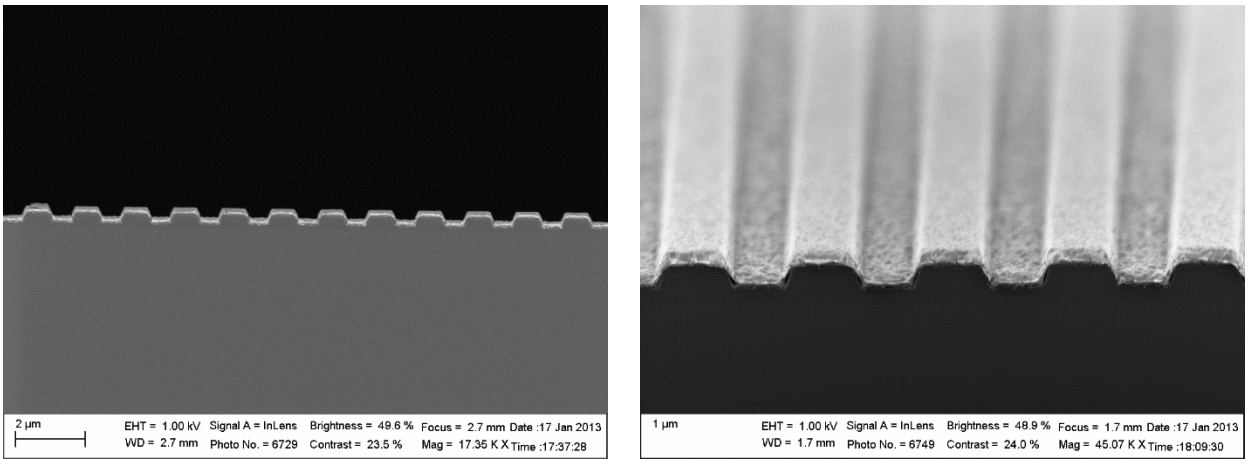

Figure 4.5-5 SEM Pictures without 5 seconds in HCl, Cross Section and 75 degree Size View

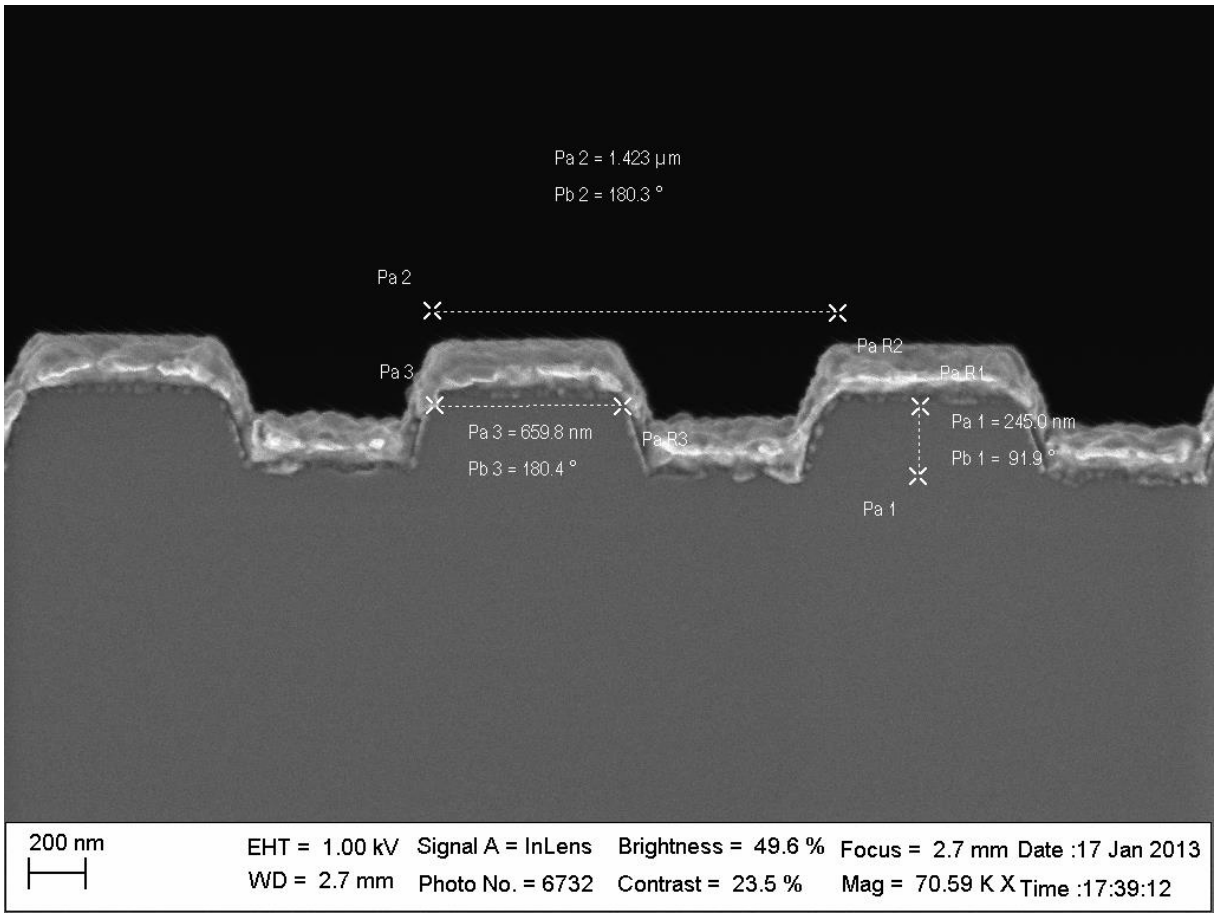

Figure 4.5-6 SEM Zoomed Pictures with 5 seconds in HCl

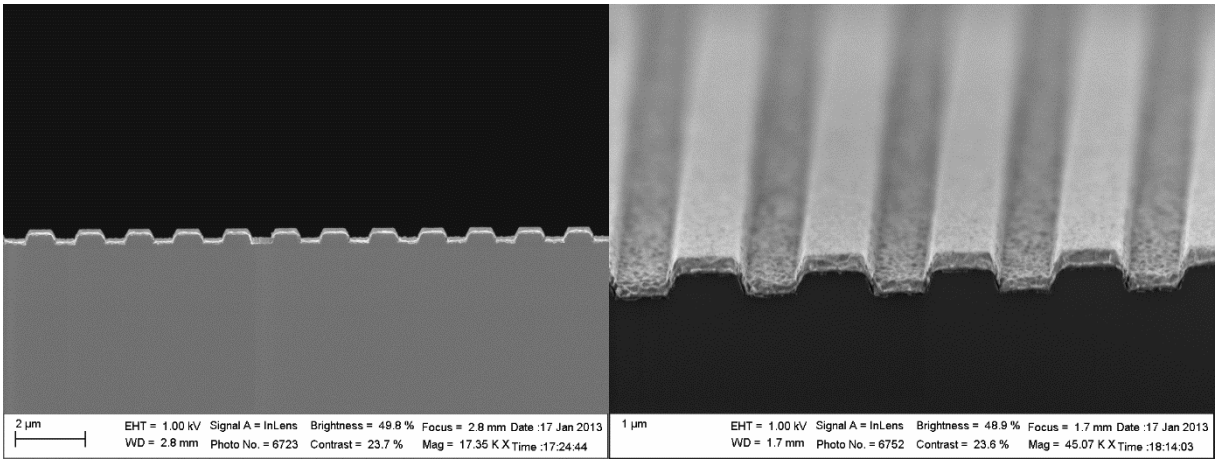

Figure 4.5-7 SEM Pictures without 15 seconds in HCl, Cross Section and 75 degree Size View

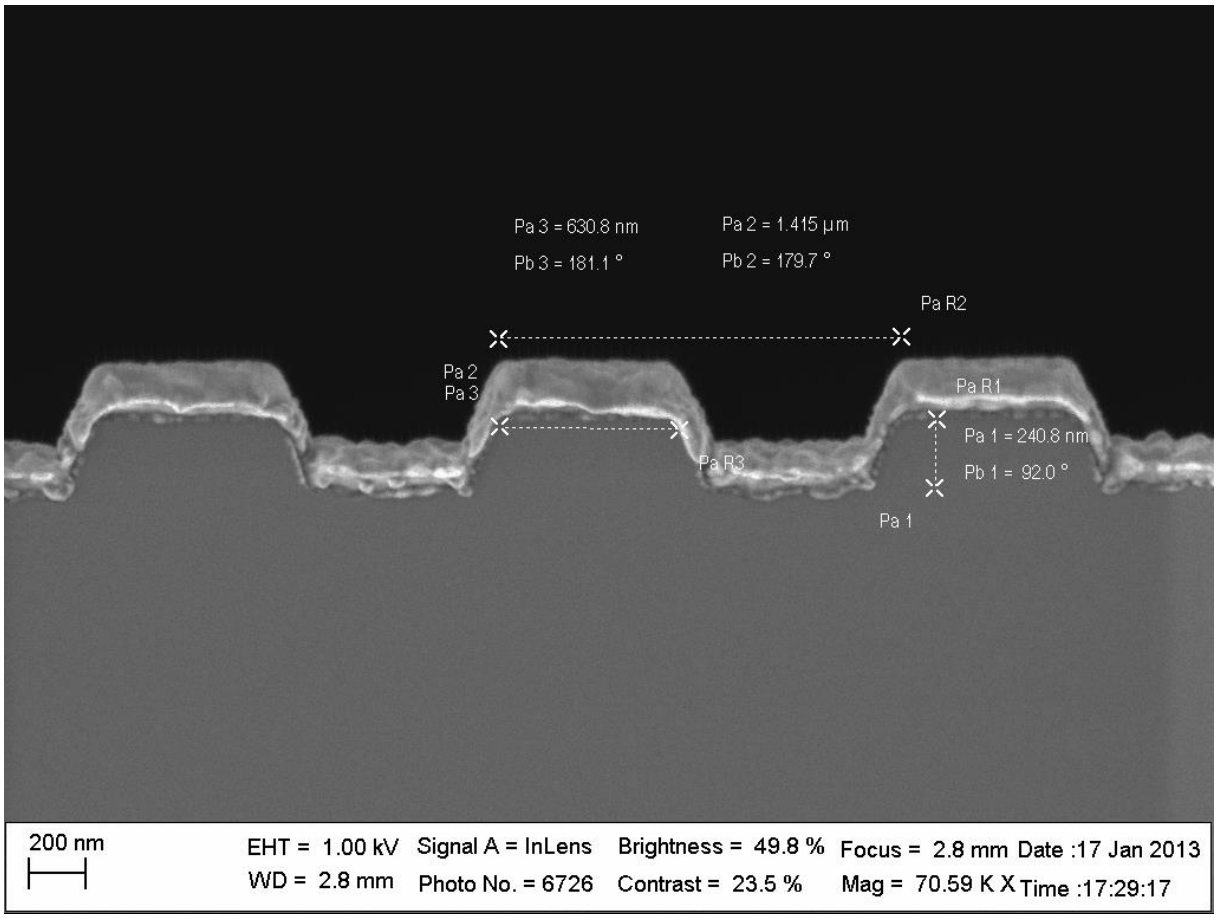

Figure 4.5-8 SEM Zoomed Pictures with 15 seconds in HCl

It is shown that sample without smoothing will have some dark regions between deposited metal and semiconductor, while it is hard to see after immersed in HCl liquid. Differences between 5 seconds and 15 seconds are not much. As to ECR etching, due to its better surface after etching, it is less necessary to soak into HCl.

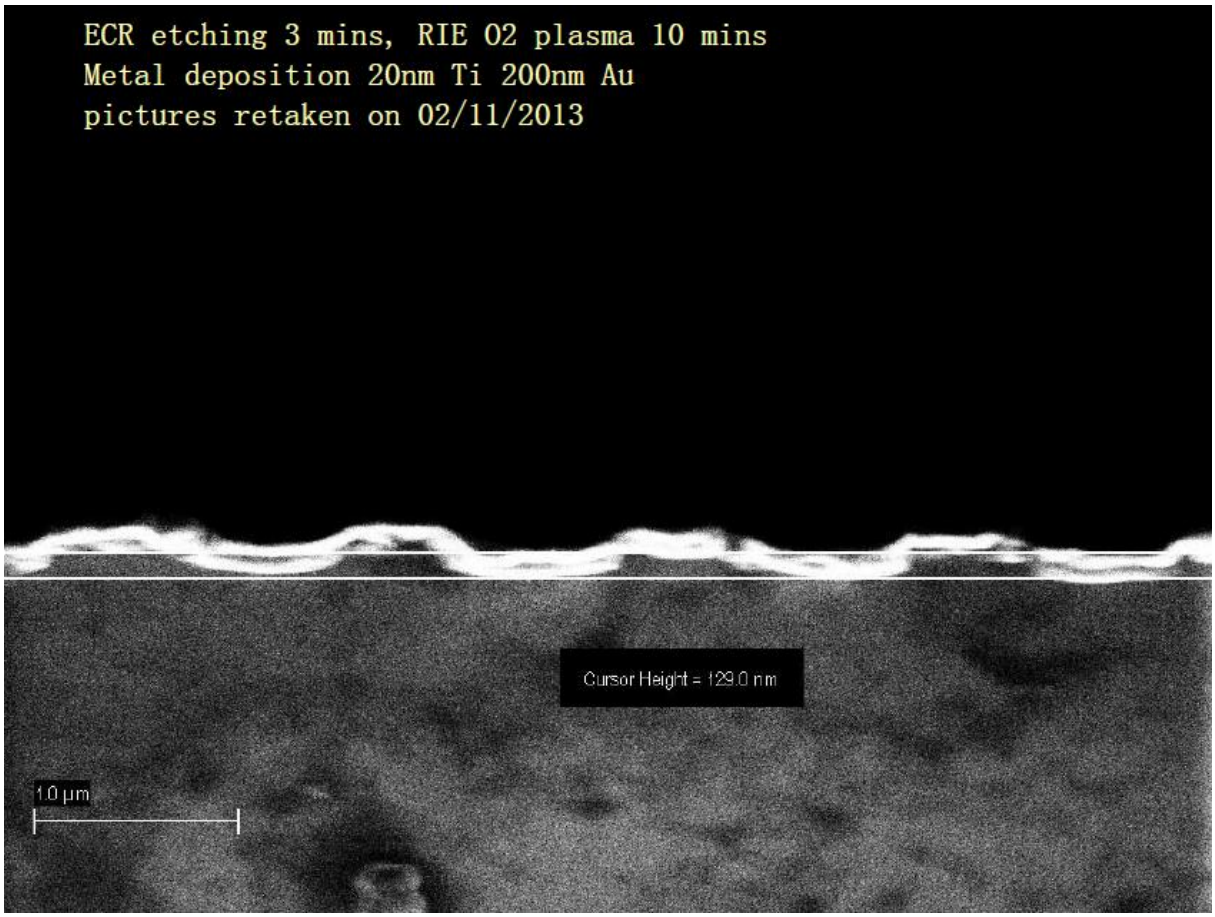

Figure 4.5-9 SEM Zoomed Pictures with 15 seconds in HCl

4.6 Conclusion

First possible future trial is that hard-mask such SiN_x may be a possible method for wet chemical etching in the future. Wet chemical etching has been tried along with plasma etching, however, due to adhesion, PMMA deposited on the highly doped InP sheds pretty quickly when immersed into acid liquid ($HCl:H_3PO_4$=1:3). Possible solutions about how to solve this problem involves trials on different recipes for spin coating and exposure time. Hard-mask has already shown good performances by wet chemical etching in similar tests in edge-emitting QCL project.

This part of work is a both learning curve and preparation for future device fabrication. It provides a great experience to understand micro-fabrication process mechanism and facilities in cleanroom. Semiconductor device fabrication is a large industry and getting understandable its step process is necessity for engineers in this area.

Chapter 5
Conclusion and Future Work

5.1 Conclusions

This work completes an introductory research for two kinds of surface emitting laser, VCSEL and SEQCL. It is a good process to get familiar with semiconductor laser basic knowledge and mechanisms for device processing. Multiple software is used during research and it helps a lot for acknowledge of electromagnetic wave propagation (reflection, absorption and coupling). Programming skills are enhanced during this time. Some tricky techniques are learnt and applied during VCSEL thermal modeling. It is a good learning curve to understand device physics and semiconductor materials processing skills.

For the VCSEL work, it gives quite a direct profile about temperature distribution inside the device. Thermal lensing effect would be a necessary consideration factor when temperature differences is more than 70K. This will lead multimode operation and may induce gain threshold burning effect (GSHB). GSHB is the reason for free carrier absorption so overall speaking, learning temperature profile inside the device is a necessity.

As to SEQCL, two sides of work has been carried on already, modeling for searching mode, threshold calculation, radiation loss and corresponding calibration for further fabrication. To better understand the trend of different grating shape influences on radiation loss, ray optics method is introduced as a promising way. Another part of work done is about preparation of

device fabrication. Etching, deposition and lithography mechanism are applied during cleanroom for calibration. Results show reliant guarantee for device design and future fabrication. Some comparison between different recipes have been tried and results are clearly shown in related chapter.

5.2 Recommended Future Work

The results presented in this thesis lead towards several possibilities in the future to deep develop surface emitting laser. From both radiation and thermal analysis perspective, SE laser can be better improved in power consumption and thermal diffusion. The author also has some his own ideas in developing laser technology.

5.2.1 Develop Beam Steering Device for VCSEL

For the VCSEL, implanting a beam steering device in the near-field will influence output light direction. This is a promising field as controlling the beam propagation can be achieved within the laser device, not by mirrors and lens outside. It would be very useful to integrate the steering device with laser active region, cladding and cavity as one whole part. Several publications have been focused on using active Plasmonics structure to achieve that.

5.2.2 Develop Wet Etching on Hard Mask

In previous preparation part, plasma etching is used as investigation of future device fabrication method. But it is also seen that plasma etching suffers either an unstable etching profile or rough etching surface. So based on this, hard mask etching is another promising method for develop a reliable, good performance way. SiNx is commonly used as the hard mask material. PECVD is mostly commonly as deposition for SiNx.

5.2.3 Develop Thermal Lensing Code for Different Modes

As mentioned in previous chapter, thermal lensing effects happen when there is temperature distribution within VCSEL or SEQCL device, where how much influence on mode profile change depends on detailed structure and material applied in modeling. To develop a

common module in commercial software with integration of overall structure would be a great idea to compact the whole analysis. Definitely this work needs time and good physics understanding, however, it would be a useful tool. What is more, heat sink is another necessary consideration in designing device.

5.2.4 More Investigation on Modeling Configuration

The author is always confused by the huge time consumed on running model. This happens both when first trial on constructing three-dimensional VCSEL thermal model and two-dimensional SEQCL array model. From the author's limited experience, it would be better to look more about high performance computing technique in modeling simulation. Mastering some skills in reducing the memory cost would be very helpful in time reduction and hardware requirement.

Bibliography

[1] Kim, Hyunsoo, Park, Seong-Ju ; Hyunsang Hwang. "Design and fabrication of highly efficient light emitting diodes", *IEEE Transactions on Electronics Devices*, OCT 2002, Vol 49, Issue 10, Nov 2002.

[2] W. A. Clarkson, N. S. Felgate, and D. C. Hanna, "Simple method for reducing the depolarization loss resulting from thermal induced birefringence in solid-state lasers," *Optics Letters*, Vol. 33, Issue 12, June 2009

[3] Scifres, D.R., "Phase-locked Semiconductor laser arrays," *Applied Physics Letters*, Vol. 76, Issue 10, March 2000

[4] Iga, K. Koyama, F. ; Kinoshita, S., "Surface Emitting Semiconductor lasers," *IEEE Journal of Quantum Electronics*, Vol. 24, Issue 9, Aug 2002

[5] Mott, J.S. ; Noll, R.J. ; Gallatin, G.M. ; Gratrix, E.J. ; ODwyer, S.L. ; Lambert, S.A., "Surface Emitting distributed feedback semiconductor laser," *Applied Physics Letter*, Vol. 51, Issue 7, June 2009

[6] Jerome Faist, Federico Capasso, *et al*, "Surface Emitting Semiconductor lasers," *Science*, Vol. 264, NO 5158, Apr 1994

[7]. Napartovich, A.P., Elkin, N.N., Vysotsky, D.V. *et al*. "Two-dimensional antiguided vertical cavity surface emitting laser arrays with reflecting boundary," *Semiconductor Laser Conference (ISLC)*, 2012 23rd IEEE International

[8] Delai Zhou and Mawst, L.J., "High-power single-mode Antiresonant reflecting optical waveguide-type vertical-cavity surface-emitting lasers," *IEEE Journal of Quantum Electronics*, Vol. 38, Issue 12, Aug 1987

[9] Delai Zhou and Mawst, L.J., "Simplified-antiresonant reflecting optical waveguide-type vertical-cavity surface-emitting lasers," *Applied Physics Letters*, Vol. 76, Issue 10, March 2000

[10] Prashant P. Baveja, Benjamin Kogel, Petter Westbergh *et al*, "Assessment of VCSEL thermal rollover mechanisms from measurements and empirical modeling," *Optics Express*, Vol. 19, NO 16, Aug 2011.

[11] Comsol Manual, Page 147-149

[12] Raffaele Colombelli, Federico Capasso and Claire Gmachl *et al*. "Far-infrared surface-plasmon quantum-cascade laser at 21.5 μm and 24 μm wavelengths," *Applied Physics Letters*, Vol. 78, Issue 18, Apr 2001.

[13] S. H. Macomber, J. S. Mott and R. J. Noll *et al.*, "Surface-emitting distributed semiconductor laser," *Applied Physics Letters*, Vol. 51, Issue 7, Aug 1987.

[14] G. Binnig, C. F. Quate and Ch. Gerber, "Principles of Distributed Feedback and Distributed Bragg-Reflector Lasers," *IEEE Journal of Quantum Electronics*, Vol. 10, Issue 4, April 1974.

[15] R. J. Noll and S. H. Macomber, "Analysis of Grating Surface Emitting Lasers," *IEEE Journal of Quantum Electronics*, Vol. 26, NO 3, March 1990.

[16] Tsung-Yu Kao, Qing Hu and John L. Reno. "Phase-locked arrays of surface-emitting terahertz quantum-cascade lasers," *Applied Physics Letters*, Vol. 96, Issue 10, Feb 2010.

[17] Guo Wan-Hong, Liu Jun-Qi, and Wang Zhan-Guo *et al.*, "Design of surface emitting distributed feedback quantum cascade lasers with single-lobe far-field pattern and high output efficiency," *Chin. Phys. B*, Vol. 19, NO 5, Oct 2009.

[18] A. Hardy, David. F. Welch and William. Streifer, "Analysis of Second Order Grating," *IEEE Journal of Quantum Electronics*, Vol. 25, NO 10, Oct 1989.

[19] Guo Wanhong, Lu Quanyong and Wang Zhanguo, "Atomic Force Microscope," *Journal of Semiconductors*, Vol. 31, NO 11, Nov 2010.

[20] Sushil Kumar, Benjamin S. Williams, Qi Qin, AlanW. M. Lee, and Qing Hu. "Surface-emitting distributed feedback terahertz quantum-cascade lasers in metal-metal waveguides," *Optics Express*, Vol. 15, NO 1, Dec 2006.

[21] M. Carras, M. Garcia, X. Marcadet and S. Bansropun, "Top grating index-coupled distributed feedback quantum cascade lasers," *Applied Physics Letters*, Vol. 93, Issue 1, June 2008

[22] D. M. Pai and K. A. Awada, "Analysis of dielectric gratings of arbitrary profiles and thickness," *J. Opt. Soc. Am*, Vol. 8, NO 5, May 1991.

[23] Wai-Hon Lee and William Streifer, "Radiation Loss Calculation for Corrugated Dielectric Waveguide," *J. Opt. Soc. Am*, Vol. 69, NO 12, Dec 1979.

[24] R. J. Shul, G. B. McClellan and R. D. Briggs, "High-density plasma etching of compound semiconductors," *Journal of Vacuum Science and Technology*, Vol. 15, Issue 3, May 1997.

[25] R. J. Shul, S. P. Kilcoyne, M. Hagerott Crawford and J. E. Parmeter, "High Temperature electron cyclotron resonance etching of GaN, InN, and AlN," *Applied Physics Letters*, Vol. 66, Issue 14, Apr 1995.

[26] G. Binnig, C. F. Quate and Ch. Gerber, "Atomic Force Microscope," *Physical Review Letters*, Vol. 56, Issue 9, Mar1986.

[27] J. Bohandy, B. F. Kim, F. J. Adrian, "Metal deposition from a supported metal film using an excimer laser," *Journal of Applied Physics*, Vol. 60, Issue 14, May 1986.